Coarse-Graining Fields in Particle-Based Soil Models

Björn Ahlman (bjnahn04@student.umu.se)

July 15, 2020

Abstract

In soil, where trees and crops grow, heavy vehicles shear and compact the soil, leading to reduced plant growth and diminished nutrient recycling. Computer simulations offer the possibility to improve the understanding of these undesired phenomena.

In this thesis, soils were modelled as large collections of contacting spherical particles using the Discrete Element Method (DEM) and the physics engine AGX Dynamics, and these entities were analyzed.

In the first part of the thesis, soils, which were considered to be continua, were subjected to various controlled deformations and fields for quantities such as stress and strain were visualized using coarse graining (CG). These fields were then compared against analytical solutions. The main goal of the thesis was to evaluate the usefulness, accuracy, and precision of this plotting technique when applied to DEM-soils. The general behaviour of most fields agreed well with analytical or expected behaviour. Moreover, the fields presented valuable information about phenomena in the soils. Relative errors varied from 1.2 to 27 %. The errors were believed to arise chiefly from non-uniform displacement (due to the inherent granularity in the technique), and unintended uneven particle distribution. The most prominent drawback with the technique was found to be the unreliability of the plots near the boundaries. This is significant, since the behaviour of a soil at the surface where it is in contact with e.g. a vehicle tyre is of interest.

In the second part of the thesis, a vehicle traversed a soil and fields were visualized using the same technique. Following a limited analysis, it was found that the stress in the soil can be crudely approximated as the stress in a linear elastic solid.

Master's Thesis in Engineering Physics, 30 credits
Supervisor: Martin Servin (UMIT, Department of Physics, Umeå University)
Co-supervisor: Viktor Wiberg (Ibid)
Examiner: Erik Wallin (Ibid)

Contents

1   Introduction

Soil mechanics is an important discipline in several scientific fields. In civil engineering, for example, structures rest on soil [1]. Trees and crops grow in soil. In agriculture and forestry, heavy vehicles shear and compact the soil, which leads to reduced plant growth and diminished nutrient recycling [7]. Experiments that increase the knowledge of soil mechanics carry the potential to e.g. mitigate compaction due to a heavy machine. Physical experiments with real vehicles, however, are cumbersome and expensive. On the other hand, computer-based simulations offer the possibility to carry out a large number of experiments with e.g. different types of terrain. In this thesis, soils were modelled as large collections of contacting spherical particles using the Discrete Element Method (DEM) and the physics engine AGX Dynamics.

Soils are distinct from other materials due to their special properties [1]. Key quantities and terms include stress, strain, shear, deformation, and dilatancy [2]—these will be explained later. When a heavy vehicle traverses a soil, it is of interest to be able to study a system of plots of quantities such as stress and strain. Such a system offers the possibility to quickly visually identify important phenomena (such as compaction), an identification that can be harder, more time-consuming, and less intuitive by studying numerical data from a simulation.

This thesis is composed of two parts. In the first part, the author evaluates a plotting technique based on coarse graining (CG) in which—due to the complexity of a particle-based soil—a simplified representation of the system of particles is generated. CG has several applications, one of which is that it is possible to obtain continuous fields (even though the particles are discrete) which describe e.g. the stress or strain in the soil, and these fields can be visualized. In order to investigate this CG plotting technique, cubical *pseudo-solids*, which we considered to be continua, were created using DEM. The difference between pseudo-soils and properly modelled soils is that the former carries zero friction, zero rolling resistance, and zero cohesion, while these quantities are non-zero for the latter. This simplified the analysis. The pseudo-soils were subjected to various deformations, and scalar and vector fields were plotted. These plots—and the numerical data which underpins the plots—were compared against analytical solutions and were examined, chiefly in terms of their general behaviours and errors*, and a conclusion was drawn regarding the usefulness and applicability of the technique. This was the main goal of the thesis. Although the evaluation of the technique applies to soils and granular materials in general, the focus was on soils stressed by heavy vehicles, and, as such, quantities that are key within that domain were prioritized. Two such key quantities are stress and strain.

In the second part, a vehicle traversed a soil, and plots were created in the same way as in the first part. A brief analysis of the fields is presented. This time, the soil had non-zero values for friction, rolling resistance, and cohesion in order to mimic real soil.

The purpose of the thesis was to improve the analysis of soil dynamics and deformations. Hopefully this can be of use to the research community and ultimately lead to a more sustainable agriculture and forestry, and the innovations of machines with lesser

---

*If we say that the general behaviour agrees well with the analytical solution, the *qualitative* agreement is good (high accuracy). If the error is low, the *quantitative* agreement is good (high precision).

environmental impact.

2 Theory

2.1 Properties of Soil

Soils are distinct from other materials due to their special properties [1]. We consider soil to be the weathered material in the upper layers of the earth's crust, for example, sand, silt, clay, or a mixture of these material. In the sections below, these special properties are explained briefly.

2.1.1 Stiffness

Materials that regain their shape after a deformation are denoted *elastic*. One example is rubber, provided that the deformation is not too large (a rubber band snaps when pulled too far). Materials that deform irreversibly after a deformation are denoted *plastic*. One example is clay. Soils have both elastic and plastic behaviour and are thusly often denoted elasto-plastic. Sometimes a soil behaves like a solid, sometimes like a fluid.

Many material, such as metals, concrete, and wood, are linear elastic and satisfy Hooke's law (up to a certain stress level). Soils do not satisfy this law and become gradually stiffer in compression, see Fig. 1. As a soil is compressed, the particles are brought closer. This increases the contacting areas, and so also the forces between the particles. For example, a coffee* package under vacuum, i.e. under high compression, is very stiff, while it becomes loose when opened.
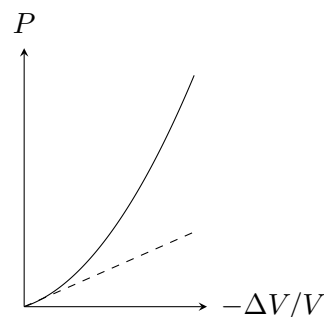
Figure 1 – Solid line: The pressure P as a function of the negative volume strain $\Delta V/V$ for a soil. Figure adapted from [3]. Dashed line: Hooke's law.

2.1.2 Shear

Shear strain is a deformation in which parallel surfaces slide past one another. In contrast to compression, in which soils become stiffer, shear softens soil [1]. At a great enough shear in relation to pressure, a soil fails. For example, the slope of a heap of sand can not exceed around 35°. This angle is known as the angle of repose, see Fig. 2.

Figure 2 – The angle of repose for a heap of sand is approximately $\phi = 35$°.

---

*Ground coffee is obviously not a soil, but has soil-like properties. Actually, ground coffee is a *granular material*, which is a conglomerate for collections of distinct macroscopic particles, to which soils belong.

2.1.3 Dilatancy

Dilatancy is defined as the volume change in a granular material (such as a soil) due to shear deformation. Loose sand has a propensity to contract, and densely packed sand can usually deform only if there is a volume expansion, see Figs. 3 and 4. This property is why the densely packed soil around a human foot on a beach dries. The weight of the foot causes shear deformation and thus volume expansion. Water is drawn into the empty region between the particles, drying the surface. Understanding of dilatancy is crucial when building heavy structures that rest of soil.

Figure 3 – Soil with particles modelled as spheres in a tightly packed state.

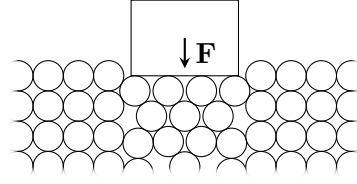**Figure 4** – Dilatancy. The load results in a shearing deformation: particle layers slide over each other, and the volume is increased.

2.2 Discrete Element Method

2.2.1 Introduction

In the Discrete Element Method (DEM), a solid is modelled using a large collection of small contacting particles. To model soil using DEM is a promising and versatile option [8]. In this paper, soils are modelled using DEM and small spherical rigid particles. It is computationally intractable to use true particle size, so instead, *pseudo-particles* are used. Such particles are larger than the real particles in a soil, so the microscopic properties of the soil are lost. The upshot is that—if the pseudo-particles are small enough, and particle parameters such as friction and rolling resistance are calibrated— the macroscopic properties of the desired soil (such as bulk cohesion and internal friction) can be obtained [9].

2.2.2 Equations of Motion

If all forces acting on particle i is known, the problem is reduced to integrating the Newton-Euler equations of motions [10]:

$$\begin{cases} m_i \ddot{\mathbf{r}}_i = \sum_c \mathbf{f}_i^c + \mathbf{f}_{\text{ext}}, \\ I_i \ddot{\boldsymbol{\varphi}}_i = \mathbf{t}_i = \sum_c \left(\mathbf{l}_i^c \times \mathbf{f}_i^c + \mathbf{q}_i^c \right), \end{cases}$$

where m_i is the mass of particle i and $\mathbf{r}_i \in \Re^{\mathcal{D}}$ its position vector, see Fig. 5. $\mathbf{f}_i^c$ are contact forces from other particles or e.g. walls, and $\mathbf{f}_{\text{ext}}$ is the sum of the external forces, e.g. gravity. I_i is the moment of inertia, $\boldsymbol{\varphi}_i \in \Re^{\mathcal{D}}$ is the angular position vector, $\mathbf{t}_i$ is torque, $\mathbf{l}_i^c$ is the vector from particle i to the particle (or object) from which $\mathbf{f}_i^c$ arises, and $\mathbf{q}_i^c$ are torques/couples at contacts other than due to a tangential force, for example

rolling or torsion. Since the particles are spherical the gyroscopic force is zero and needs not be included.

The equations of motion are thus a system of $\mathcal{D} + \mathcal{D}(\mathcal{D} - 1)/2$ coupled ordinary differential equations to be solved in $\mathcal{D}$ dimensions.
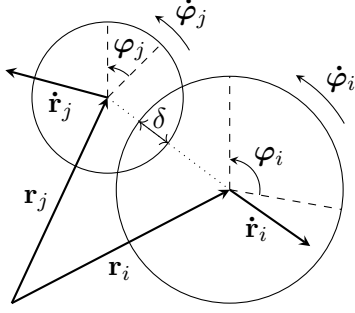
Figure 5 – Particles i and j in contact (with a contact overlap δ) and selected particle variables illustrated.
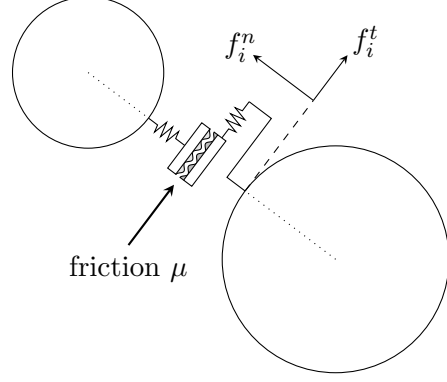
Figure 6 – Same as Fig. 5, but now the particles have been separated for a visual representation of the contact force on i due to j, which includes the normal force f_i^n (represented to arise from spring) and the tangential force f_i^t (represented to arise from a spring and the friction between two surfaces).

2.2.3 Normal and Tangential Force

The spherical particles are rigid, but can overlap, which results in normal and tangential forces. These forces can be modelled in a number of ways. The models of interest are [19]:

$$\begin{cases} f^n = k_n \delta^{3/2} + k_n c_d \sqrt{\delta} \dot{\delta}, \\ f^t = \min\left(\mu f_n, k_t \delta_t\right) = \min\left(\mu f_n, k_t \int \dot{\delta}_t dt\right), \qquad f^t \leq \mu f^n, \end{cases}$$

where the normal force f^n is a non-linear Hertz-Mindlin model with contact overlap δ, and the tangent force f^t is a linear spring-force with Coulomb condition (friction coefficient μ) and tangential slip rate $\dot{\delta}_t$, where

$$\begin{cases} k_n = \frac{E\sqrt{2d}}{3(1-\nu^2)}, \\ c_d = \frac{4\left(1-\nu^2\right)(1-2\nu)\eta}{15E\nu^2}, \end{cases}$$

where E is the Young modulus, ν is the Poisson ratio, η is the material viscosity constant, and d is the particle diameter.

2.2.4 Rolling Resistance, Cohesion, and Cohesive Overlap

Particles in contact subject each other to torques through friction. In modelling soil, a *rolling resistance* is often introduced. It usually takes the form of an inequality constraint: if the torque does not exceed a certain magnitude, determined by a rolling

resistance coefficient μ_r, no rolling occurs. A greater μ_r implies a stronger tendency to resist rolling.

Particles in a soil tend to stick together due to cohesion. This phenomenon is usually implemented as an inequality constraint, governed by a cohesion coefficient c_p. A greater c_p implies stronger forces between the particles and a stronger soil. The *cohesive overlap* δ_c determines the required particle overlap for cohesion to occur.

2.3 Continuum Mechanics

2.3.1 Overview

In continuum mechanics, matter is distributed continuously in a *continuum*. Quantities such as density, displacement and velocity vary continuously such that their derivatives exist and are continuous. For example, in general, mass density is defined as mass m divided by volume V. In continuum mechanics, due to the assumed continuity of matter, mass density is defined by [12]:

$$\rho \equiv \lim_{\Delta V \to \epsilon^3} \frac{\Delta m}{\Delta V},$$

where we take the limit $\epsilon \to 0$. This limit enables us to specify the density (and other quantities) at a *point* in a continuum.

Obviously, real materials are discontinuous, since the mass density in a small volume enclosing a molecule is higher than between molecules (where, in fact, the density is zero, discounting quantum mechanics), but in the macroscopic domain continuum mechanics can be a useful approximation. In this thesis, soils were modelled as collections of small spherical particles using DEM, and these samples were approximated as continua.

2.3.2 Fundamental Quantities

Consider an arbitrary body $\mathcal{B}$ of known geometry in three-dimensional Euclidean space $\Re^3$ in an arbitrary reference configuration κ_0 at time $t = 0$, see Fig. 7. We let the body undergo a deformation, which results in the configuration κ at some later time $t > 0$. The mapping $\boldsymbol{\chi}$ is the deformation mapping of $\mathcal{B}$ from κ_0 to κ, which describes the motion of $\mathcal{B}$. $\mathbf{X} = (X_1, X_2, X_3)$ is the position vector for a particle in the reference configuration, where X_i are *material* coordinates and $\mathbf{x} = (x_1, x_2, x_3)$ is the position vector in the deformed configuration, where x_i are *spatial* coordinates [13]. The separation vector between two particles, known as a material line, is in κ_0 given by $d\mathbf{X}$, and in κ by $d\mathbf{x}$. The displacement vector for a particle is defined by $\mathbf{u} \equiv \mathbf{x} - \mathbf{X}$.
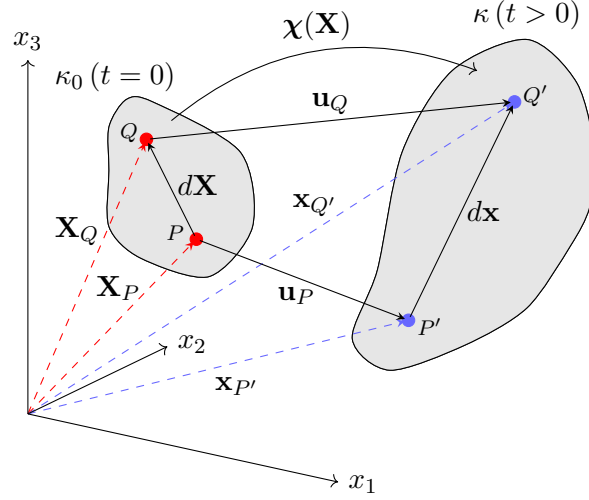
Figure 7 – A body $\mathcal{B}$ in a reference configuration κ_0 at time $t = 0$, and in a deformed configuration κ at some later time $t > 0$. Two particles P and Q in $\mathcal{B}$ are highlighted. In κ_0 they are indicated in red, and in κ, the same two particles are indicated in blue.

In the *Lagrangian* description, the motion of the body is referred to the reference configuration κ_0 and consequently current coordinates ($\mathbf{x} \in \kappa$) are expressed in terms of the reference coordinates ($\mathbf{X} \in \kappa_0$), and in the *Eulerian* description, the the motion is referred to the current configuration κ [14]. We let λ be some scalar or vector function of interest (perhaps the scalar field of the temperature in $\mathcal{B}$). Then,

$$\begin{cases} \text{Lagrangian description}: & \mathbf{x} = \boldsymbol{\chi}(\mathbf{X}, t), & \mathbf{x} = \mathbf{x}(\mathbf{X}, t), & \lambda = \lambda(\mathbf{X}, t), \\ \text{Eulerian description}: & \mathbf{X} = \boldsymbol{\chi}^{-1}(\mathbf{x}, t), & \mathbf{X} = \mathbf{X}(\mathbf{x}, t), & \lambda = \lambda(\mathbf{x}, t). \end{cases}$$

2.3.3 Velocity

Velocity in continuum mechanics is defined in a straight-forward manner:

$$\mathbf{v} \equiv \frac{d\mathbf{x}}{dt}. \tag{1}$$

2.3.4 Displacement

The displacement field for the two different descriptions are

$$\begin{cases} \text{Lagrangian description}: & \mathbf{u}(\mathbf{X}, t) = \mathbf{x}(\mathbf{X}, t) - \mathbf{X}, & \text{(2a)} \\ \text{Eulerian description}: & \mathbf{u}(\mathbf{x}, t) = \mathbf{x} - \mathbf{X}(\mathbf{x}, t). & \text{(2b)} \end{cases}$$

So, if we desire to know the displacement at some time $t = t_1$, we can either use Eq. (2a) and plug in the position vector at $t = 0$, i.e. $\mathbf{X}$, or use Eq. (2b) and plug in the position vector at t_1, i.e. $\mathbf{x}$.

2.3.5 Deformation Gradient

In continuum mechanics, two key quantities are the material line and its transformation $d\mathbf{X} \to d\mathbf{x}$ (in rigid-body mechanics, $d\mathbf{X} = d\mathbf{x}$ for any motion). The *deformation gradient* $\mathbf{F}$ of κ relative to the original configuration κ_0 gives the relationship between $d\mathbf{X}$ and $d\mathbf{x}$ [15]:

$$d\mathbf{x} = \mathbf{F} \cdot d\mathbf{X} = d\mathbf{X} \cdot \mathbf{F}^T. \tag{3}$$

From this, we obtain

$$\mathbf{F} = \left(\frac{\partial \boldsymbol{\chi}}{\partial \mathbf{X}}\right)^T = \left(\frac{\partial \mathbf{x}}{\partial \mathbf{X}}\right)^T \equiv (\nabla_0 \mathbf{x})^T, \qquad F_{ij} = \begin{pmatrix} \frac{\partial x_1}{\partial X_1} & \frac{\partial x_1}{\partial X_2} & \frac{\partial x_1}{\partial X_3} \\ \frac{\partial x_2}{\partial X_1} & \frac{\partial x_2}{\partial X_2} & \frac{\partial x_2}{\partial X_3} \\ \frac{\partial x_3}{\partial X_1} & \frac{\partial x_3}{\partial X_2} & \frac{\partial x_3}{\partial X_3} \end{pmatrix},$$

where ∇_0 is the gradient operator with respect to $\mathbf{X}$. The deformation gradient, a second order tensor, can also be expressed in terms of the displacement vector:

$$\begin{cases} \mathbf{F} = (\nabla_0 \mathbf{x})^T = (\nabla_0 \mathbf{u} + \mathbf{I})^T, & \text{(4a)} \\ \mathbf{F}^{-1} = (\nabla \mathbf{X})^T = (\mathbf{I} - \nabla \mathbf{u})^T, & \text{(4b)} \end{cases}$$

where $\mathbf{I}$ is the identity matrix, and ∇ is the gradient operator with respect to $\mathbf{x}$.

2.3.6 Strain

Strain is the deformation in a continuous body with respect to the relative displacement of particles (and is thus independent of translation and rotation). Expressions for strain are obtained by considering the materials lines. We have, by Eq. (3):

$$\begin{cases} (ds)^2 = d\mathbf{x} \cdot d\mathbf{x}, \\ (dS)^2 = d\mathbf{X} \cdot d\mathbf{X} = d\mathbf{x} \cdot \left(\mathbf{F}^{-T} \cdot \mathbf{F}^{-1}\right) \cdot d\mathbf{x} \equiv d\mathbf{x} \cdot \widetilde{\mathbf{B}} \cdot d\mathbf{x}, \end{cases}$$

where $\widetilde{\mathbf{B}}$ is the *Cauchy strain tensor*. Moreover, we can write $(ds)^2 - (dS)^2 = 2d\mathbf{x} \cdot \mathbf{e} \cdot d\mathbf{x}$, where $\mathbf{e}$ is the *Euler strain tensor* [16]:

$$\mathbf{e} = \frac{1}{2}\left(\mathbf{I} - \mathbf{F}^{-T} \cdot \mathbf{F}^{-1}\right).$$

Then, by Eqs. (4a) and (4b):

$$\mathbf{e} = \frac{1}{2}\left[\nabla \mathbf{u} + (\nabla \mathbf{u})^T - (\nabla \mathbf{u}) \cdot (\nabla \mathbf{u})^T\right]. \tag{5}$$

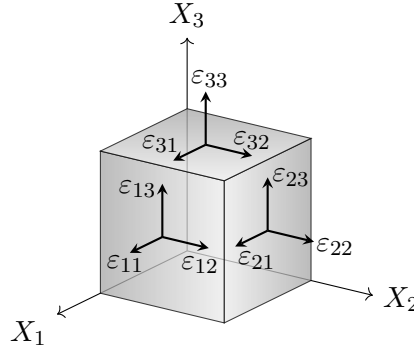### 2.3.7 Infinitesimal Strain Tensor

If $|\mathbf{u}| \ll 1$, we can neglect the second order term in Eq. (5). This yields the *infinitesimal strain tensor*:

$$\varepsilon = \frac{1}{2}\left[\nabla \mathbf{u} + (\nabla \mathbf{u})^T\right], \qquad \varepsilon_{ij} = \frac{1}{2}\left(\frac{\partial u_i}{\partial x_j} - \frac{\partial u_j}{\partial x_i}\right), \qquad |\mathbf{u}| \ll 1. \tag{6}$$

In expanded form:

$$\varepsilon = \begin{pmatrix} \varepsilon_{11} & \varepsilon_{12} & \varepsilon_{13} \\ \varepsilon_{21} & \varepsilon_{22} & \varepsilon_{23} \\ \varepsilon_{31} & \varepsilon_{32} & \varepsilon_{33} \end{pmatrix} = \begin{pmatrix} \frac{\partial u_1}{\partial X_1} & \frac{1}{2}\left(\frac{\partial u_1}{\partial X_2} + \frac{\partial u_2}{\partial X_1}\right) & \frac{1}{2}\left(\frac{\partial u_1}{\partial X_3} + \frac{\partial u_3}{\partial X_1}\right) \\ \frac{1}{2}\left(\frac{\partial u_2}{\partial X_1} + \frac{\partial u_1}{\partial X_2}\right) & \frac{\partial u_2}{\partial X_2} & \frac{1}{2}\left(\frac{\partial u_2}{\partial X_3} + \frac{\partial u_3}{\partial X_2}\right) \\ \frac{1}{2}\left(\frac{\partial u_3}{\partial X_1} + \frac{\partial u_1}{\partial X_3}\right) & \frac{1}{2}\left(\frac{\partial u_3}{\partial X_2} + \frac{\partial u_2}{\partial X_3}\right) & \frac{\partial u_3}{\partial X_3} \end{pmatrix}.$$

We note that no distinction is made between the material coordinates $\mathbf{X}$ and the spatial coordinates $\mathbf{x}$ in the infinitesimal strain tensor. The normal strain ε_{ij} $(i = j)$ is the ratio of change in length of a line element that was parallel to the x_i-axis in the undeformed body to its original length. The shear strain ε_{ij} $(i \neq j)$ corresponds to the change in angle between line elements that were perpendicular to each other in the undeformed body. In Fig. 8 the infinitesimal strain tensor is visualized.

Figure 8 – The infinitesimal strain tensor visualized. The component ε_{ij} acts on a surface perpendicular to the i-axis. The surfaces at $X_i > 0$ represent planes that goes through a point, and ε_{ij} pertains to that point.

The total volume strain, i.e. total change in volume, is given by the trace of the infinitesimal strain tensor [4]:

$$\frac{\Delta V}{V} = \text{tr } \varepsilon. \tag{7}$$

tr $\varepsilon > 0$ indicates expansion, while tr $\varepsilon < 0$ indicates compression.

2.3.8 Stress

Stress is force per unit area. Consider an arbitrary continuous body subjected to some contact (or external) force field $\mathbf{F}$, see Fig. 9. Following Euler's equations of motions, internal forces are transmitted from point to point in the body, yielding the internal force field $\mathbf{f}$. We let $\Delta\mathbf{f}(\hat{\mathbf{n}})$ denote the force on a small area Δa inside the body with arbitrary orientation and unit normal $\hat{\mathbf{n}}$. We define the stress vector:

$$\mathbf{t}^{(\hat{\mathbf{n}})} \equiv \lim_{\Delta a \to 0} \frac{\Delta\mathbf{f}(\hat{\mathbf{n}})}{\Delta a}.$$
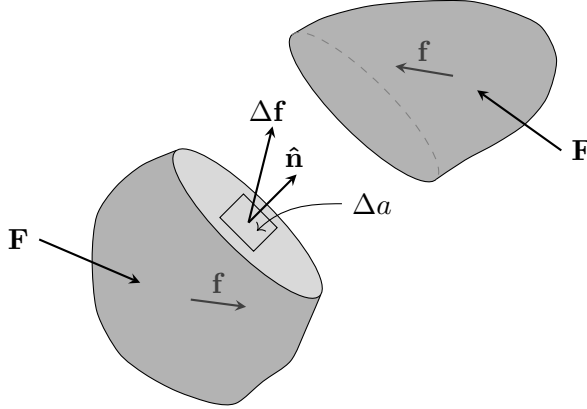
Figure 9 – An arbitrary continuous body, illustrating the force $\Delta\mathbf{f}$ on a small area segment Δa. For visual clarity, the body has been split into two at a plane in which Δa lies.
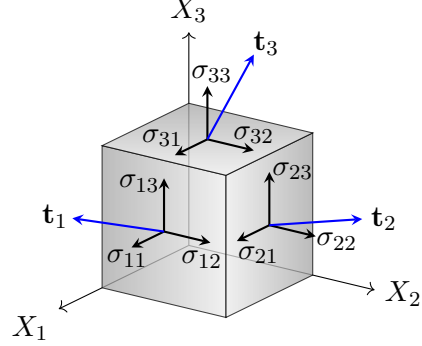
Figure 10 – The Cauchy stress tensor visualized. The component σ_{ij} acts on a surface perpendicular to the i-axis, and is due to some force $\mathbf{t}_i$. The surfaces at $X_i > 0$ represent planes that goes through a point, and σ_{ij} acts on that point.

According to Cauchy's Fundamental Lemma (or, equivalently, according to Newton's third law): $-\mathbf{t}^{(\hat{\mathbf{n}})} = \mathbf{t}^{(-\hat{\mathbf{n}})}$. The state of stress at a point in the body is defined by the stress vectors $\mathbf{t}^{(\hat{\mathbf{n}})}$ associated with all planes that pass through that point. According to Cauchy's stress theorem, there exists a second-order tensor field $\boldsymbol{\sigma}(\mathbf{x}, t)$, the *Cauchy stress tensor* (see Fig. 10), that is independent of $\hat{\mathbf{n}}$, and which can be related to $\mathbf{t}^{(\hat{\mathbf{n}})}$ such that $\mathbf{t}^{(\hat{\mathbf{n}})}$ is a linear function of $\hat{\mathbf{n}}$ [17]:

$$\mathbf{t}^{(\hat{\mathbf{n}})} = \boldsymbol{\sigma} \cdot \hat{\mathbf{n}}, \qquad T_{ij}^{(n)} = \sigma_{ij}\hat{n}_i.$$

In expanded form:

$$\begin{pmatrix} t_1 \\ t_2 \\ t_3 \end{pmatrix} = \begin{pmatrix} \sigma_{11} & \sigma_{12} & \sigma_{13} \\ \sigma_{21} & \sigma_{22} & \sigma_{23} \\ \sigma_{31} & \sigma_{32} & \sigma_{33} \end{pmatrix} \begin{pmatrix} \hat{n}_1 \\ \hat{n}_2 \\ \hat{n}_3 \end{pmatrix}.$$

Using the Cauchy stress tensor, we define pressure (or mean normal stress):

$$P \equiv -\frac{1}{3}\mathrm{tr}\left(\boldsymbol{\sigma}\right).$$

2.3.9 Constitutive Equations

A constitutive equation describes the relation between quantities that is specific to a material. One such equation is Hooke's law, which describes the stress-strain relationship for a particular material. The generalized Hooke's law, applicable for linear elastic solids, is given by [18]:

$$\sigma_{ij} = C_{ijkl}\varepsilon_{kl},$$

where $C_{ijkl} = \partial^2 U_0/\partial\varepsilon_{mn}\partial\varepsilon_{ij}$, and U_0 is the strain energy density function such that $\sigma_{ij} = \partial U_0/\partial\varepsilon_{ij}$. In the one-dimensional case, the equation reduces to the more common form $F = -kx$.

Soil, however, do not in general obey Hooke's law, as described in Section 2.1.1.

2.3.10 Relationship Between Stress and Strain

The Young modulus is a measure of the stiffness of a material. It is defined as

$$E \equiv \frac{\sigma}{\varepsilon},$$

where σ is uniaxial stress, and ε is strain (change in length divided by original length).

2.3.11 Stress in a Linear Elastic Material

Consider a homogeneous isotropic linear elastic half space $(-\infty < x, y < \infty, -\infty < z < 0)$. Gravity points in the negative z-direction. If we place a circular plate at the origin with its axis parallel to the z-axis, the static normal vertical stress at a point z is given by [6]

$$\sigma_{zz} = P \left[1 - \left(\frac{|z|}{A - z^2} \right)^3 \right], \qquad x = y = 0,$$

where P is the pressure exerted on the material from the plate, and A is the area of the plate.

This stress was compared against the experimental stress for the vehicle on soil.

2.3.12 Analytical Expressions for Deformations

For the investigation of the CG plotting script, cubical pseudo-solids were modelled as collections of spherical particles, and the solids were considered to be continua. These solids then underwent four different types of deformations—deformations that increase linearly with time, with the exception of deformation due to gravity, which is non-linear with respect to time. These deformations are described analytically in this section, using the Lagrangian description. Isotropic compression is described in Fig. 11.


(a) Initial state.   (b) Final state.   (c) Displacement vector field.
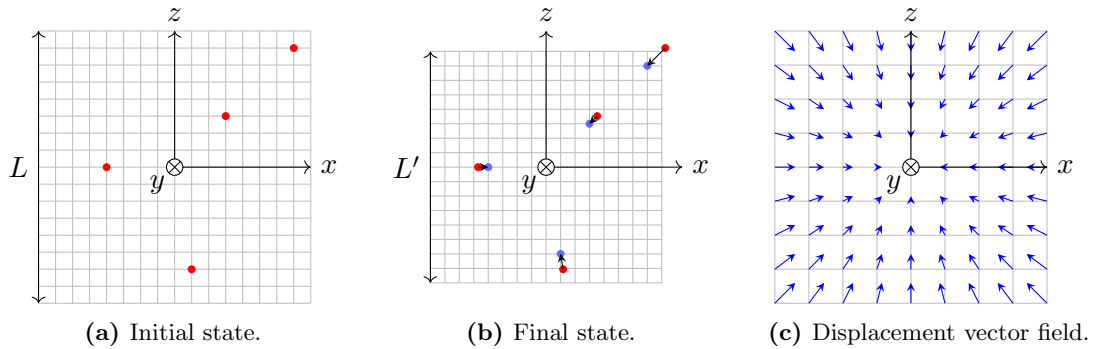
Figure 11 – Isotropic compression of a cubical solid (represented by a grid) in 3D. Plots in the xz-plane. The final compression is 15% in the x-, y-, and z-directions.

In Fig. 11.a, the initial state is given in which the solid is undeformed. The red dots indicate the position of a few material elements in the undeformed solid. In Fig. 11.b, the final state is given in which the solid is deformed. The blue dots indicate the

positions of the same material elements in the deformed solid.For reference, the positions of the elements in the undeformed body is also given. The black vectors indicate the displacement for these elements. In Fig. 11.c, the blue vectors give the displacement for the deformation over the entire solid.

Triaxial deformation is described in Fig. 12.

(a) Initial state.   **(b)** Final state.   **(c)** Displacement vector field.
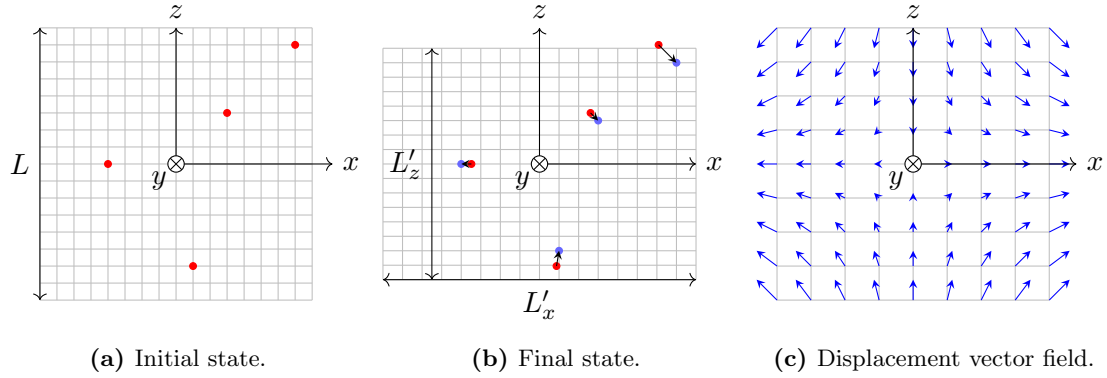
Figure 12 – Triaxial deformation. Plots in the xz-plane. In the x-direction the final *expansion* is 15%, and in the y- and z-directions the final *compression* is 15%.

Simple shear deformation is described in Fig. 13.

(a) Initial state.   **(b)** Final state.   **(c)** Displacement vector field.
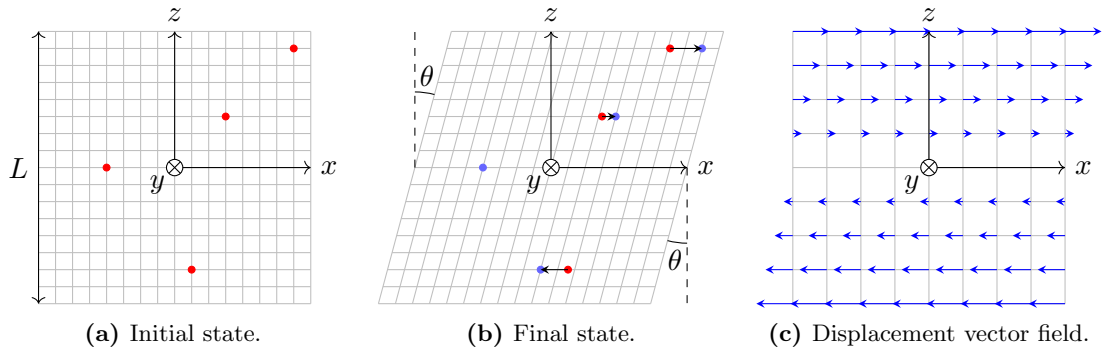
Figure 13 – Simple shear deformation, with final angle $\theta = 15°$. Plots in the xz-plane. The lines in the body remain parallel (and the distance between them are constant) during the deformation, but they are translated. (If a small angle is used, this test is linear, since, in the Maclaurin expansion of $\tan \theta$ to the first non-zero term: $\tan \theta \cong \theta$.)

Deformation due to gravity is described in Fig. 14.

13

(a) Initial state.   **(b)** Final state.   **(c)** Displacement vector field.
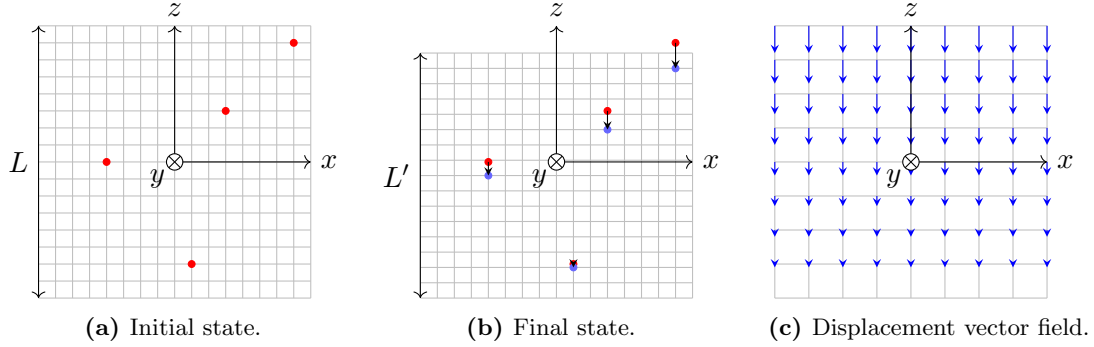
Figure 14 – Deformation due to gravity. Plots in the xz-plane.

In Fig. 14, we assume that stress and strain are linearly proportional for the material of the solid. Material elements near the bottom experience a large stress and strain, while elements near the top experience a small stress and strain. Then, the compression is linearly proportional to z, in accordance with Archimedes' principle.

The analytical displacements, strain tensors and volume strains for these four deformations are detailed in the Appendix, see Section A.1.

2.4 Coarse Graining

2.4.1 Introduction

At the bulk level, a particle based material appears solid and it is therefore meaningful to estimate continuous fields such mass density, displacement, stress, etc. [20], and to plot these fields. Coarse graining (CG) is a projection process in which a macroscopic description is obtained from the microscopic description of the pseudo-particles. CG has several applications, one of which is that it enables plotting of continuous fields. The macroscopic scale is defined by a CG scale R, usually related to the particle diameter d^*. The macroscopic fields are computed with the aid of a CG function. There are several alternatives for this function. The selected one is Gaussian[†], defined by [21]

$$\phi(\mathbf{x}) \equiv \frac{1}{\left(\sqrt{2\pi}R\right)^3}\exp\left(-|\mathbf{x}|^2/2R^2\right), \qquad \int_{\text{all space}} \phi(\mathbf{x})dx = 1,$$

where $\mathbf{x} \in \Re^3$ is the coordinate point. Using the CG function and the variables of the particles (e.g. position and velocity) in a neighbourhood of $\mathbf{x}$, we can define fields.

2.4.2 Definition of Fields

We define the *mass density* scalar field

$$\rho(\mathbf{x}, t) \equiv \sum_a m^a \phi\left(\mathbf{x} - \mathbf{X}^a\right), \tag{8}$$

---

[*]If particles have different radii, a weighted average can be used for d.

[†]A Gaussian function results in smooth fields and is infinitely differentiable. Another possibility is to use Lucy polynomials.

where m^a and $\mathbf{X}^a$ are the mass and position, respectively, of the particles in the neighbourhood. The coordinate point $\mathbf{x}$ is a continuous variable so ρ is a *continuous* field (as are all fields presented below).

We define the *velocity* vector field

$$\mathbf{v}(\mathbf{x}, t) \equiv \mathbf{p}(\mathbf{x}, t)/\rho(\mathbf{x}, t),$$

where $\mathbf{p} = \sum_a m^a \mathbf{V}^a \phi\left(\mathbf{x} - \mathbf{X}^a\right)$ is the *momentum density* vector field, and $\mathbf{V}^a$ are the velocities of the particles.

In the quasi-static regime, the *stress tensor* is approximately equal to the *contact stress tensor* [21]

$$\sigma_{\alpha\beta}\left(\mathbf{x}, t\right) \cong - \sum_a f_{\alpha,n}^{ab} x_\beta^{ab} \int_0^1 \phi\left(\mathbf{x} - \mathbf{X}^a(t) + s\mathbf{x}^{ab}(t)\right) ds, \qquad (9)$$

where the summation is over the set of contacts, $\mathbf{f}_n^{ab}$ is the contact force between particles a and b, with branch vector $\mathbf{x}^{ab} \equiv \mathbf{X}^b - \mathbf{X}^a$. The spatial components of the tensor is indexed by $\alpha, \beta, \ldots$, ranging $1, 2, 3 = x, y, z$ (using the Einstein summation convention).

Pressure, or mean normal stress, is given by

$$P(\mathbf{x}, t) = -\frac{1}{3}\mathrm{tr}\left(\sigma_{\alpha\beta}\right).$$

The *displacement* vector field is given by

$$\mathbf{u}(\mathbf{x}, t) \equiv \frac{\sum_a m^a \mathbf{U}^a \phi(\mathbf{x} - \mathbf{X}^a(t))}{\rho(\mathbf{x}, t)},$$

where $\mathbf{U}^a \equiv \mathbf{X}^a(t) - \mathbf{X}^a(0)$.

The *linear strain tensor* is given by

$$\varepsilon_{\alpha\beta}(\mathbf{x}, t) \equiv \frac{1}{2}\left(F_{\alpha\beta} + F_{\beta\alpha}\right),$$

where the *deformation gradient* is [22]

$$F_{\alpha\beta} \equiv \frac{\partial u_\alpha}{\partial x_\beta} = \frac{\sum_a \sum_b m^a m^b \left(u_\alpha^a - u_\alpha^b\right)\left(\partial_\beta \phi^a\right)\phi^b}{\rho(\mathbf{x}, t)^2},$$

where $\phi^a \equiv \phi\left(\mathbf{x} - \mathbf{X}^a(t)\right)$, and $\phi_\beta \phi^a \equiv \partial\phi^a/\partial x_\beta$.

The *rate of strain* tensor is given by

$$\dot{\varepsilon}_{\alpha\beta}(\mathbf{x}, t) = \frac{1}{2}\left(\widetilde{F}_{\alpha\beta} + \widetilde{F}_{\beta\alpha}\right),$$

where $\widetilde{F}_{\alpha\beta}$ is the gradient of the velocity vector field:

$$\widetilde{F}_{\alpha\beta} \equiv \frac{\partial v_\alpha}{\partial x_\beta} = \frac{\sum_a \sum_b m^a m^b \left(v_\alpha^a - v_\beta^b\right)\left(\partial_\beta \phi^a\right)\phi^b}{\rho(\mathbf{x}, t)^2}.$$

We define the *power density* scalar field

$$S(\mathbf{x}, t) \equiv \sigma_{\alpha\beta}\dot{\varepsilon}_{\alpha\beta},$$

which yields the time rate of energy transfer (power) per unit volume.

2.4.3   Implementation

The fields in Section 2.4.2 are continuous. However, it is computationally intensive to calculate the fields at a vast number of points. Therefore, we place the system of particles in a three-dimensional voxel grid, see Fig. 15. At the center of each voxel, the value of the field of interest is calculated. Consider voxel i. All particles within radius $|\mathbf{x}| = 3R$, i.e. three times the CG scale, contribute to the field (light blue spheres), while all the particles outside this sphere do not (light gray spheres), in order to improve computational time (the contributions from the particles outside this radius are negligible). Thus, to each voxel, there is a list in which the particles within radius $3R$ and their contact points are stored. This yields discretized fields, with field values at a reasonable number of points from a computational standpoint. For a scalar field, we obtain a dataset in which there is value associated with the center of each voxel, see Fig. 16 (for a vector field, a set of components is associated with each voxel center).

To acquire smooth plots, interpolation is applied to the datasets. Methods include bilinear, bicubic, and nearest neighbour interpolation. Bicubic interpolation is selected since it carries greater smoothness and less interpolation distortion, although the method is slower [23].

The program that implements the CG fields and produces these plots is denoted the *CG plotting script**. A typical relation between the CG scale R, voxel size L, and particle diameter d is $R = 2L = 1.5d$.
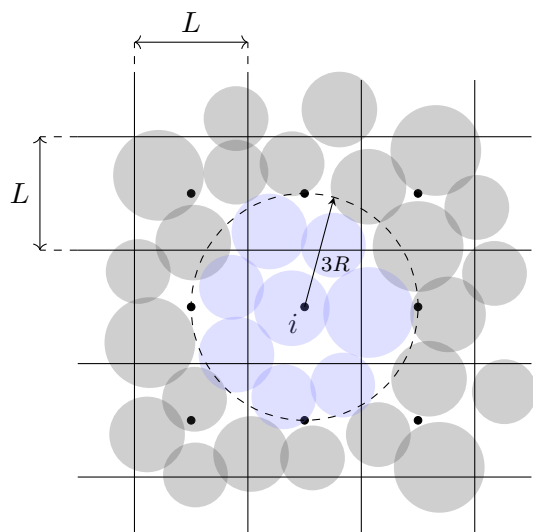
Figure 15 – A voxel grid with voxel width and height L over a system of spherical particles. At the center of each voxel, the field value is calculated. At each voxel center, only the particles inside a sphere of radius $3R$ contribute to the field.

Figure 16 – A value (perhaps the mass density) assigned to the center of each voxel for a scalar field.

---

*Developed chiefly by M. Servin, E. Wallin, and T. Berglund, with minor contributions from the author.

The evaluation of the stress, Eq. (9), is simplified by using a Heaviside kernel function and only considering the contact points within a cube of side $2L$, but this function will not be detailed.

2.5 Statistics

We let the true value of some quantity be x_{true}, and the measured value be x_{meas}. Then, the absolute and relative errors are defined as [27]:

$$\begin{cases} \epsilon_{\text{abs}} \equiv x_{\text{meas}} - x_{\text{true}}, & \text{(10a)} \\[2mm] \epsilon_{\text{rel}} \equiv \dfrac{x_{\text{meas}} - x_{\text{true}}}{x_{\text{true}}}. & \text{(10b)} \end{cases}$$

We define the standard deviation s as

$$s \equiv \sqrt{\frac{1}{N-1} \sum_{i=1}^{N} |A_i - \mu|^2}, \qquad \mu \equiv \frac{1}{N} \sum_{i=1}^{N} A_i,$$

where N are the number of observations A_i, and μ is the arithmetic mean.

3 Method

3.1 Cubical Tests

3.1.1 Creation of Test Samples

For the creation of the test samples, collections of pseudo-particles were created within the confines of six walls that overlapped and met at right angles, see Figs. 17[*] and 18[†] (the walls could only collide with the particles and not with each other). These samples were created in a gravity-free environment, and there was no friction, cohesion, or rolling resistance, neither for the walls nor the particles. For more details, see the Appendix, Section A.2.
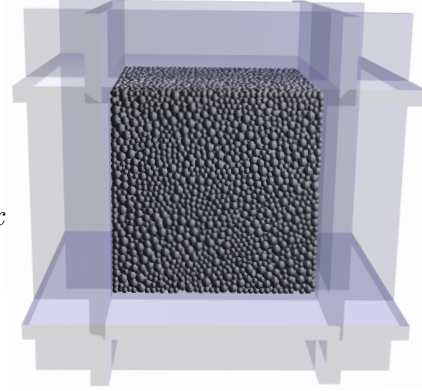
---

[*]A modified version of a sample creation program created by V. Wiberg.
[†]Sample creation program created by V. Wiberg.
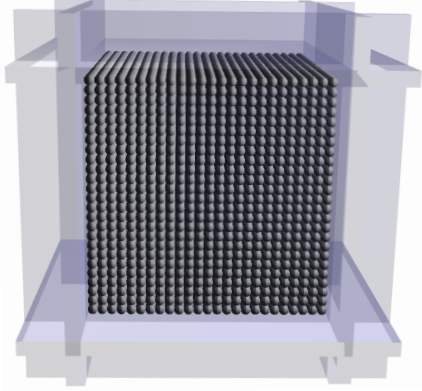
Figure 17 – A cubic test sample of dimensions $1.0 \times 1.0 \times 1.0$ m, centered at the origin, consisting of 15625 particles of radius 2 cm in a primitive cubic formation. Pressure at walls is 0 kPa.

Figure 18 – A cubic test sample of dimensions $0.86 \times 0.86 \times 0.86$ m, centered at the origin, consisting of 24764 particles in a randomised configuration. The particles have three different radii: 2.0, 1.7, and 1.2 cm. Pressure at walls is 1.0 kPa.

These two different test samples served different purposes. The sample with randomised configuration and different radii was modelled to resemble soil[*], so the tests of that sample resembled tests of a soil and was thus the most important test sample. However, due to the random configuration, it is difficult to control the dynamics of the particles during a test, which in turn imposes challenges when interpreting the results. Now, the sample with the simple cubic formation was not modelled to mimic soil. However, the dynamics of the particles in that sample are easier to control (provided that the cubic formation is maintained). Consequently, tests on that sample yielded results which were easier to compare with e.g. analytical results, and were useful to determine numerical precision.

3.1.2   Tests of Samples

The test samples were then subjected to various tests[†], for example isotropic compression (in which all six walls move towards the center of the sample, compressing it), or a gravitational test (in which gravity is activated for the particles, but not the walls, compressing the sample). All tests are listed in the next section. The CG plotting script, see Section 2.4, was appended to the tests and plots of e.g. density, strain, and stress were created every $10th$ timestep (250 times/s). These plots and the underlying numerical data were then evaluated, chiefly in terms of general behaviour and numerical precision. The setup for the voxel grid is given in Fig. 19. The evaluation was focused on comparing obtained results and expected results. For example, to evaluate the result for pressure plot, the applied forces from the AGX motors were studied; to evaluate the result for the mass density plot, the mass and volume of the sample were inspected.

---

[*]The authors in the following article use the same approach to model soil: [8].

[†]Modified versions of a program created by V. Wiberg.

The number of comparisons were more than a few and they were diverse, so they are detailed in connection with the pertinent results in order to prevent disorientation, i.e. in Sections 4 and A.
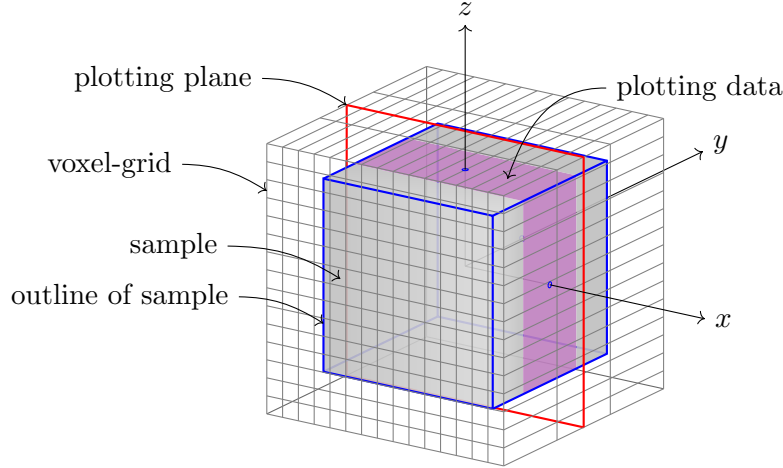
Figure 19 – A cubical test sample in a voxel-grid. The number of voxels in the x-, y-, and z-direction are $\{N, 3, N\}$, where e.g. $N = 50$. The plotting plane is the xz-plane ($y = 0$), and the data used for the plots lies in the region indicated in violet (i.e. the center y-voxel, and all voxels in the x- and z-directions). Three voxels (and not more) are used in the y-direction to reduce computational time. A single voxel in the y-direction would entail an undesired inclusion of empty space, since the voxel grid extends beyond the sample.

3.1.3 List of Tests

A total of six tests were carried out:

(i) Isotropic compression—particles in random configuration: all six walls move towards the center of the sample, compressing it.

(ii) Isotropic compression—particles in cubic formation.

(iii) Gravitational test—particles in random configuration: gravity is activated for the particles, but not the walls, compressing the sample.

(iv) Gravitational test—particles in cubic formation.

(v) Triaxial test—particles in random configuration: the top and bottom walls compress the sample, while the other four walls move away from the sample.

(vi) Simple shear test—particles in random configuration: the left and right walls rotate about their centers, shearing the sample.

3.2 Vehicle on Soil

In the second part of the thesis, a vehicle traversed a soil, and fields were visualized using CG*. This soil was created in the same way as the test soil in random configuration was

---

*The vehicle and the soil used are the same as those used and/or created by the authors in the following article: [8].

created, but here, the particles had friction, rolling resistance, and cohesion, in order for the soil to mimic real soil.

For the plotting, we placed the plotting grid directly below the front wheel at each timestep, letting the grid follow the vehicle. In Fig. 20, the vehicle at some time t_0 is shown. The red and blue rectangles indicate plotting grids. In Fig. 21, the vehicle at some later time $t_1 > t_0$ is shown. So the fields were constantly plotted directly under the front wheel. In the horizontal dimensions, the centers of the plotting grids were located at the mass center of the front wheel. To mitigate fluctuations in the fields, we then took the average of the fields. The plots from the beginning and the end of the run, where the vehicle was close to the vertical boundaries, were not included in the averaging.

The fields were then briefly analyzed. In particular, we evaluated how well the normal stress in the vertical direction agrees with the analytical stress in a linear elastic solid.
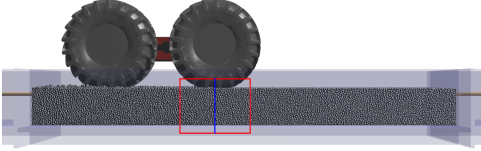
Figure 20 – The vehicle as some time t_0. The red and blue rectangle indicates the plotting grid in the xz and yz-plane, respectively.
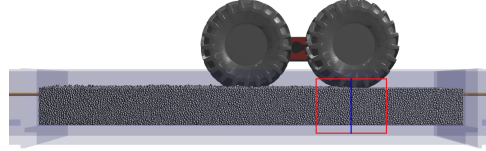
Figure 21 – The vehicle as some time $t_1 > t_0$.

3.3 AGX Dynamics

3.3.1 Overview

As described in Section 2.2.2, DEM yields a system of equations to be solved in order to obtain the equations of motions. In this thesis, the numerical integration and simulations of the particle systems were carried out by the physics engine AGX Dynamics, which implements a hybrid solver (a combination of direct and iterative solvers) [24]. The direct one is a Mixed Linear Complementarity Problems (MLCP) solver. The iterative one is a block sparse projected Gauss-Seidel (GS) solver, and also MLCP. The GS solver is fast on large contact systems [25], making it an appropriate choice, since there is a vast number of particle contacts in a large DEM-system. DEM is computationally intensive, so AGX implements the Nonsmooth Discrete Element Method (NDEM), in which collisions and stick-slip transitional events are approximated as instantaneous, allowing for a larger timestep, yielding less computational time [26]. Technical details will be omitted.

3.3.2 Size of Timestep and Number of Iterations

In the quasi-static regime, for an error tolerance ϵ, the timestep should be chosen such that the following holds [8]:

$$\Delta t \lesssim \sqrt{2\epsilon d/\dot{v}_n},$$

where d is the particle diameter, $\dot{v}_n \approx \sigma A_p/m_p$ is the acceleration of the particle, where σ is the characteristic stress, A_p the particle great circle cross-sectional area, and m_p the

particle mass. Also, for the same error tolerance ϵ, the number of iterations should be selected such that the following holds:

$$N_{\text{it}} \gtrsim 0.1n/\epsilon,$$

where n is the length of the contact network (number of particles) in the direction in which the dominant stress acts.

4 Results

4.1 Sample Testing

In this section, the result from the CG plotting script for an isotropic compression test with particles in a random configuration are presented. For all tests, the setup for the voxel grid and plotting plane is given in Fig. 19. Also, the relation $R = 2L = 1.5d$ was used consistently, see Section 2.4.3. For solids with different radii, the weighted average was used for d. The timestep and number of iterations were selected such that the numerical error should not exceed 0.01.

In the Appendix, the results from five more tests are given: an isotropic compression test with particles in a simple cubic formation (Section A.4.5); a gravitational test with particles in simple cubic formation (Section A.4.6); a gravitational test with particles in primitive cubic formation (Section A.4.6); a triaxial test with particles in a random configuration (Section A.4.8); a shear test with particles in random configuration (Section A.4.9). For technical details of the tests, such as particle radii, values for the Young moduli, etc., see the Appendix, Table 2.

4.1.1 Isotropic Compression Test—Particles in Random Configuration

In this test, the test sample was first loaded into the test-script, see Fig. 22, and the walls were held static for 0.5 s, allowing for any motion of the particles in the test sample to subside. Subsequently, all six walls were accelerated slowly towards the origin using virtual motors which could supply an (essentially) infinite amount of force. The speed was increased linearly with 0.01 cm/s each timestep. The left and right walls were constrained to have only translational motion along the x-axis (similarly, the back and front walls moved along the y-axis, and the top and bottom walls moved along the z-axis). Thus the right angles between the walls were maintained. When a wall moving in direction i $(i = x, y, z)$ reached the speed 2.5 cm/s (at $t = 0.6$ s) that speed was maintained until the compression reached 3% along direction i, upon which that wall was set static. When the compression criterion was reached for all three directions, the test finished, see Fig. 23.
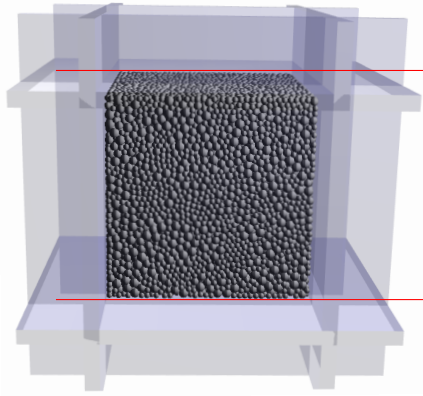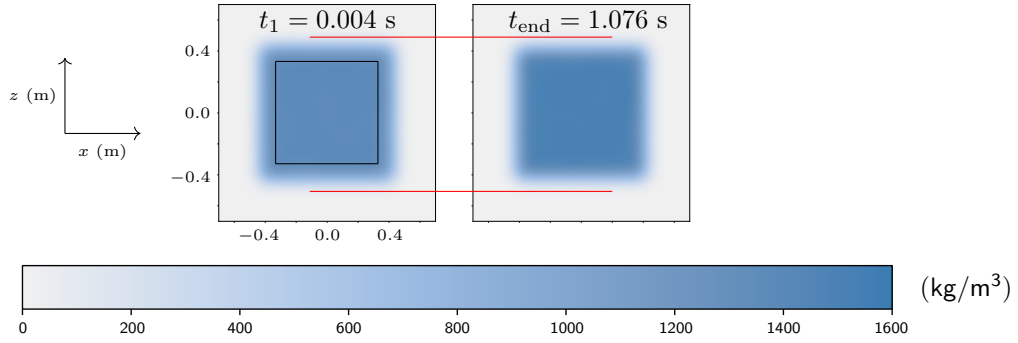
Figure 22 – The test sample at $t = 0$ s (same as Fig. 18).
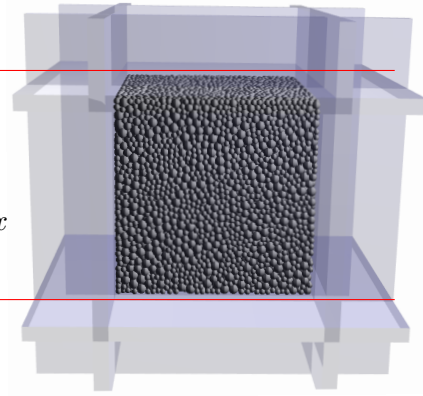
Figure 23 – The test sample at $t = 1.076$ s (compression complete). The red horizontal reference lines facilitate the recognition of the compression.

Throughout this section, bicubic interpolation is used for the scalar field plots. The results for the mass density are given in Fig. 24.


Figure 24 – The mass density at time t_1 (the beginning) and at t_{end} (compression complete). The black square indicates a region in which an average was calculated.

At the start of the test, the average mass density for the sample was kg/m^3, which seems to be in agreement with Fig. 24. At the end of the test, the plot is of a slightly darker blue and slightly smaller, indicating an expected increase in density and decrease in volume. Notice the fadings near the boundaries, indicating a smooth decrease in density. This is a boundary effect due to the averaging nature of the CG technique. In reality, the density obviously decreases sharply at the boundary, since there are no particles outside the walls. Now, a narrower interval for the density would reveal existing fluctuations in the density, but this would introduce stronger boundary effects, see the Appendix, Section A.4.4. A way around this is to use contour lines, which are used for the Vehicle on Soil, see Section 4.3.

Boundary effects can be handled by adding correction terms [29]. Such terms will not be covered in this thesis.

Now, by consulting the data produced by AGX (the mass of the sample, and the positions of the walls), we calculated the expected density as a function of time. We

denote this function ρ_{AGX}. Moreover, we let ρ_{CG} denote the average* of the density, based on the numerical data underlying the CG plots. The two functions are compared in Fig. 25. By *assuming* that ρ_{AGX} is the true density, we obtain, by Eqs. (10a) and (10b), the absolute and relative errors for ρ_{CG} as functions of time. These errors are given in Figs. 26 and 27.
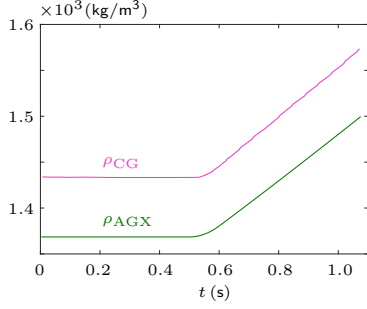
Figure 25 – Mass densities ρ_{AGX} and ρ_{CG}.
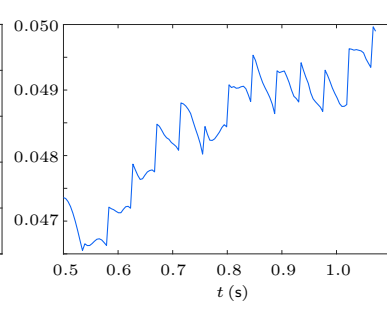
Figure 26 – Estimated relative error $\epsilon_{\text{rel}}(\rho_{\text{CG}})$ for ρ_{CG}.
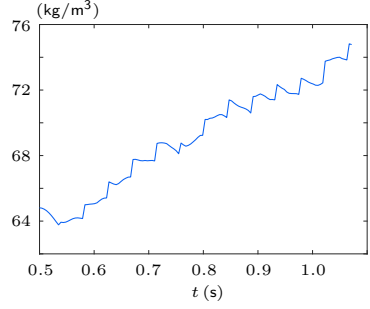
Figure 27 – Estimated absolute error $\epsilon_{\text{abs}}(\rho_{\text{CG}})$ for ρ_{CG}.

The average of the *magnitude* of the relative errors is

$$\bar{\epsilon}_{\text{rel}}(\rho_{\text{CG}}) = 0.049 \pm 0.001, \qquad t > 0.6 \text{ s},$$

where the value after $\pm$ is the standard deviation of the relative errors.

We note that the general behaviour of ρ_{CG} follows that of ρ_{AGX} very well. Also, the relative error is considered small. Actually, since we average over a region inside the walls, we expect ρ_{CG} to be slightly higher than ρ_{AGX}, since, at the boundaries, the particles were less densely packed than in the averaged region.

Results for the particle displacement $\mathbf{u}$ and its components are given in Fig. 28.
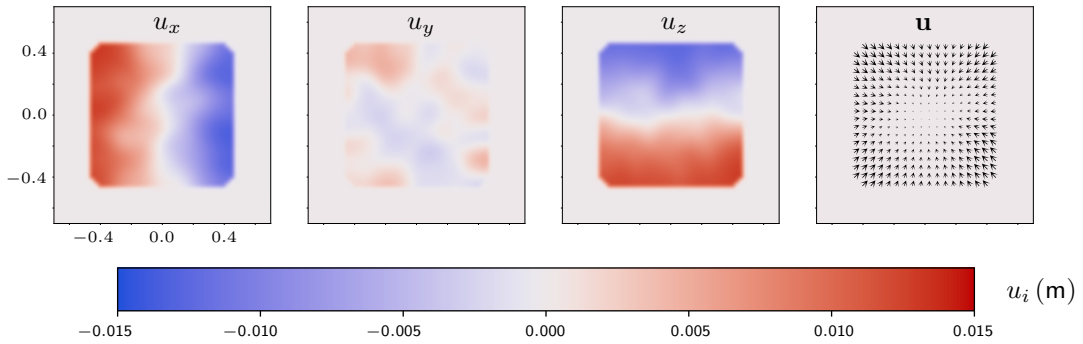
Figure 28 – The magnitude and the components of the particle displacement $\mathbf{u}$ at $t = 1.076$ s (compression complete). Horizontal axis: x (m), vertical axis: z (m).

---

*By average, we consistently indicate arithmetic mean. The averaged volume is centered about the center of the sample, and is indicated with a black square in Fig. 24. To avoid boundary effects, we stay away from the boundaries. Whenever a variable carries the subscript "CG", the average is always taken over such a black square, unless otherwise specified.

By studying Eq. (11a), and the analytical vector function in Fig. 11, we see that the plots in Fig. 28 agree with the expected behaviour quite well. Since the plotting plane is the xz-plane, we expect u_y to be zero.

Results for the particle velocity $\mathbf{v}$ and its components are given in Fig. 29.
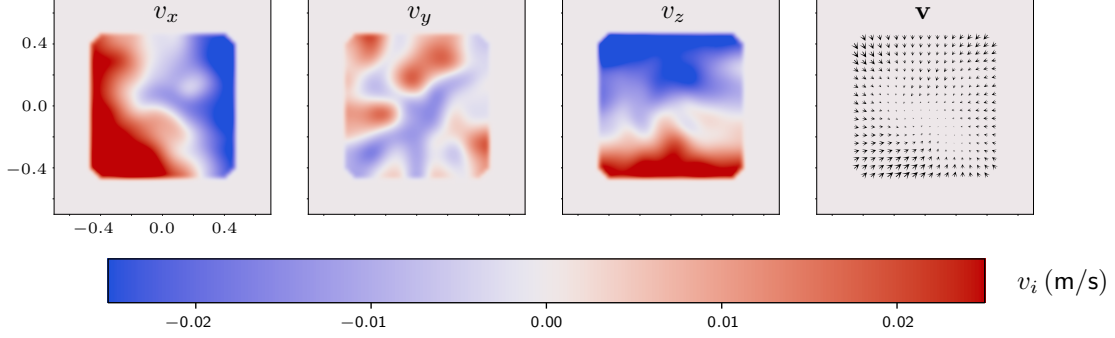
Figure 29 – The magnitude and the components of the particle velocity $\mathbf{v}$ at $t = 1.076$ s (compression complete). Horizontal axis: x (m), vertical axis: z (m).

By Eq. (12a), $\mathbf{v}$ should have the same linear behaviour as $\mathbf{u}$. Overall, the plots in Fig. 29 exhibit expected behaviour, but there are distinct fluctuations.

By Eq. (11a) we constructed the analytical expression for u_x as a function of x and denote this function $u_{x,\mathrm{ana}}$. Also, we compute the average* of u_x, given by the CG data, and denote this function $u_{x,\mathrm{CG}}$. We plot $u_{x,\mathrm{ana}}$ and $u_{x,\mathrm{CG}}$ in Fig. 30. In a similar manner, by Eq. (12a), we constructed $v_{x,\mathrm{ana}}$ and $v_{x,\mathrm{CG}}$ and plot these functions in Fig. 31. By assuming that $u_{x,\mathrm{ana}}$ and $v_{x,\mathrm{ana}}$ are the true functions, we compute the relative errors for $u_{x,\mathrm{ana}}$ and $v_{x,\mathrm{ana}}$ and plot these errors in Fig. 32.
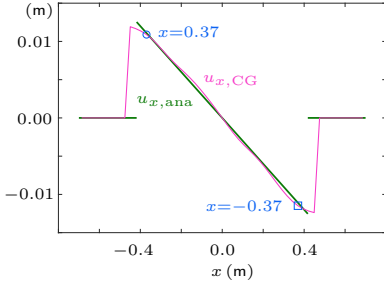
Figure 30 – Displacement components $u_{x,\mathrm{ana}}$ and $u_{x,\mathrm{CG}}$ at $t = 1.076$ s.
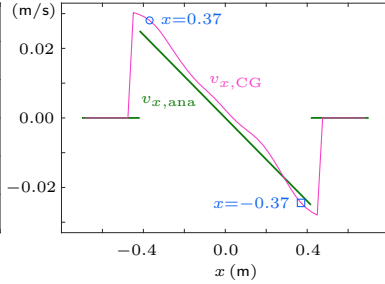
Figure 31 – Velocity components $v_{x,\mathrm{ana}}$ and $v_{x,\mathrm{CG}}$ at $t = 1.076$ s.
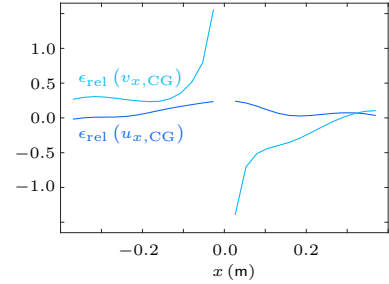
Figure 32 – Estimated relative errors $\epsilon_{\mathrm{rel}}(u_{x,\mathrm{CG}})$ and $\epsilon_{\mathrm{rel}}(v_{x,\mathrm{CG}})$ for $u_{x,\mathrm{CG}}$ and $v_{x,\mathrm{CG}}$, respectively.

If Figs. 30 and 31, the boundary effects are apparent. We consider the intervals between the blue circle and square to be largely devoid of boundary effects. The average of the

---

*The width (along z) of the averaged section is the same as given in Fig. 24.

magnitude of the relative errors* are

$$
\begin{cases}
\overline{\epsilon}_{\text{rel}}\left(u_{x,\text{CG}}\right) = 0.025 \pm 0.030, & -0.37 < x < 0.37 \text{ (m)}, \\
\overline{\epsilon}_{\text{rel}}\left(v_{x,\text{CG}}\right) = 0.12 \pm 0.08, & -0.37 < x < 0.37 \text{ (m)}.
\end{cases}
$$

$u_{x,\text{CG}}$ agrees with $u_{x,\text{ana}}$ quite well, and its relative error is small. $v_{x,\text{CG}}$ does not agree with $v_{x,\text{ana}}$ equally well, and its relative error is larger.

The distance from the blue circle (or square) to the boundary is 4.8 cm, which corresponds to $2.7r$, where r is the weighted average radius of the particles, indicating that results are unreliable within that distance from a boundary.

Results for the components of the stress tensor σ_{ij} and the pressure P are given in Fig. 33.
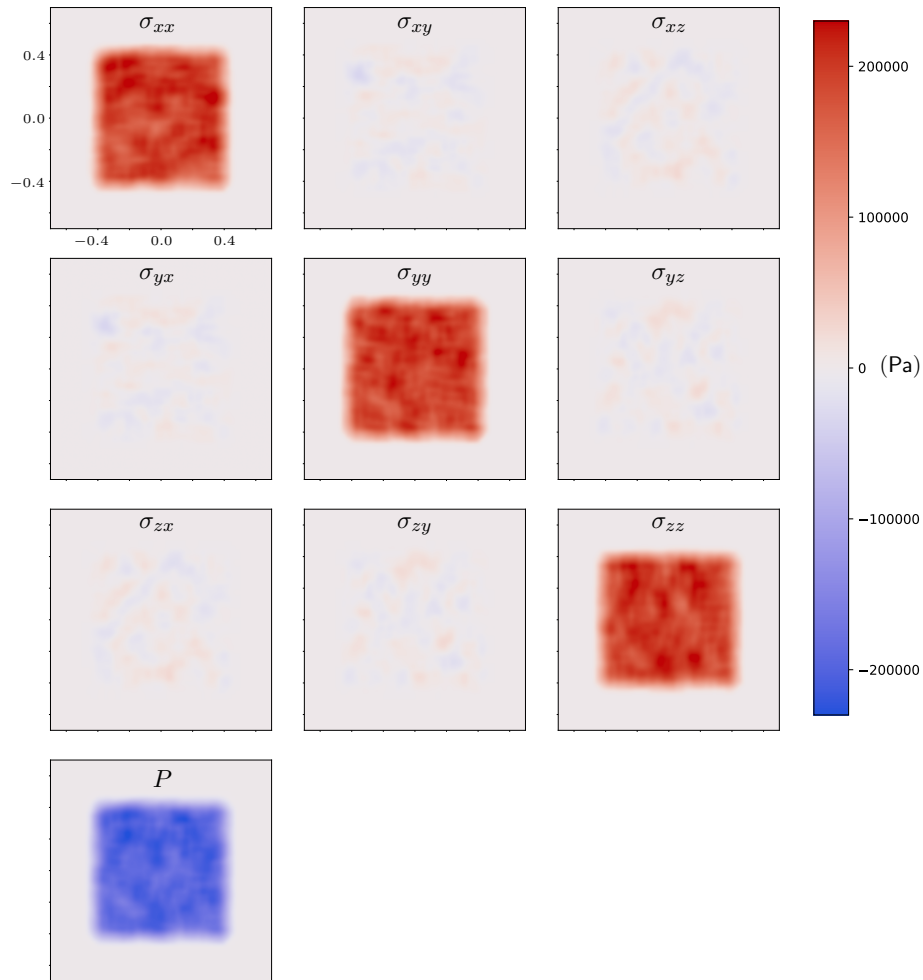
Figure 33 – The components of the stress tensor σ_{ij}, and the pressure P, at $t = 1.076$ s (compression complete). Horizontal axis is x (m), vertical axis is z (m).

---

*Since the relative error is infinite at $x = 0$, we use $\max(u_{x,\text{ana}})$ and $\max(v_{x,\text{ana}})$ for $\overline{\epsilon}_{\text{rel}}\left(u_{x,\text{CG}}\right)$ and $\overline{\epsilon}_{\text{rel}}\left(v_{x,\text{CG}}\right)$, respectively, in the denominator in Eq. (10b), i.e. as references.

Since each compressing wall was constrained to move along the x-, y-, or z-direction, we expect σ_{ij} $(i = j)$ to be uniform, and σ_{ij} $(i \neq j)$ to be zero, see Fig. 10. This is largely also what is seen in Fig. 33.

By consulting the data produced by AGX, we calculated the expected pressure within the sample as a function of time and denote this function P_{AGX} (for the derivation, see the Appendix, Section A.4.1). Moreover, we let P_{CG}* denote the magnitude of the average pressure within the sample based on the numerical data underlying the CG plots. In Fig. 34 we plot these two functions against each other. We *assume* that P_{AGX} gives the true value for the pressure. We thus obtain estimated absolute and relative errors for P_{CG}, see Fig. 35 and 36.
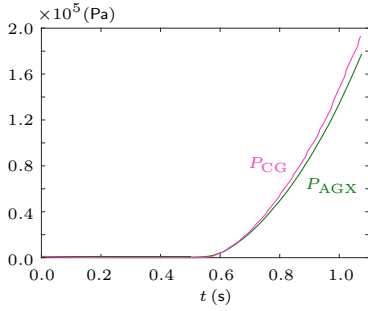
Figure 34 – Pressures P_{AGX} and P_{CG}.
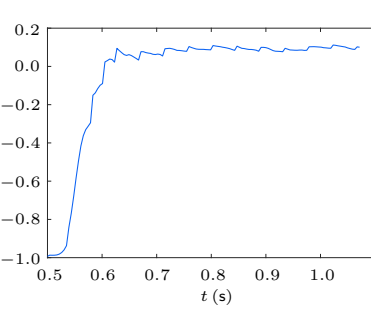
Figure 35 – Estimated relative error $\epsilon_{\text{rel}}(P_{\text{CG}})$ for P_{CG}.
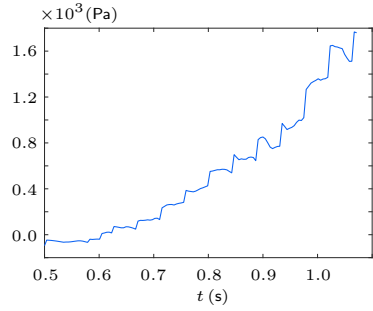
Figure 36 – Estimated absolute error $\epsilon_{\text{abs}}(P_{\text{CG}})$ for P_{CG}.

We take the average of the magnitude of the relative errors at $t > 0.6$ and obtain

$$\bar{\epsilon}_{\text{rel}}\left(P_{\text{CG}}\right) = 0.085 \pm 0.025, \qquad 0.6 \text{ s} < t.$$

We note that P_{CG} follows the behaviour of P_{AGX} quite closely, and the relative error is quite low. Plots for the average of σ_{xy}, σ_{xz} and σ_{yz} are given in Fig. 37. In the analytical case, these quantities are zero. In Fig. 37, they are non-zero. However, the experimental magnitudes are not large, compared to σ_{ij} $(i = j)$. The magnitudes of σ_{ij} $(i \neq j)$ are a few percent of the magnitudes of σ_{ij} $(i = j)$.

The results for the infinitesimal strain tensor ε_{ij} are given in Fig. 38.
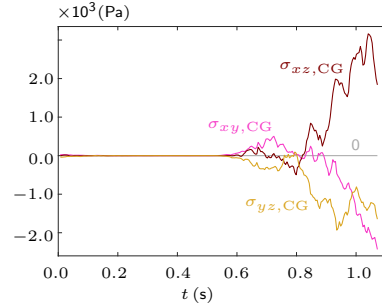
Figure 37 – Components $\sigma_{ij,\text{CG}}$ $(i \neq j)$ with a reference line at 0 Pa.

*As before, the black square in Fig. 24 indicates the averaged region.
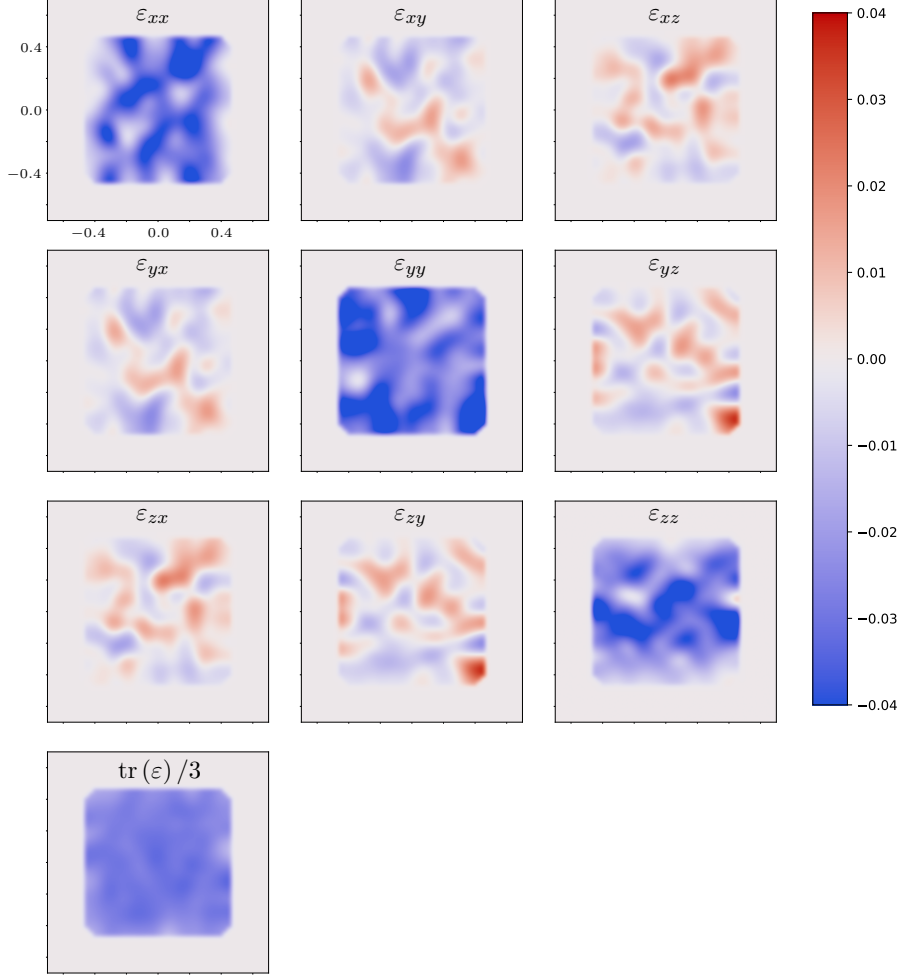
Figure 38 – The components of the infinitesimal strain tensor ε_{ij}, and the mean of ε_{ij} ($i = j$), i.e. $\mathrm{tr}\,(\varepsilon)/3$, at $t = 1.076$ s (test complete). Horizontal axis is x (m), vertical axis is z (m).

We note that the plots in Fig. 38 agree quite well with Eq. 13a. However, compared to the results for the stress tensor, the non-diagonal components present larger values (relative to the diagonal components).

We let $\mathrm{tr}\,(\varepsilon)_{\mathrm{CG}}$ denote the average of $\mathrm{tr}\,(\varepsilon)$ based on the data from CG. By storing the positions of the walls (given by AGX) at each timestep, we computed the volume of the sample as a function of time and thus also the total volume strain. We denote this volume strain $\mathrm{tr}\,(\varepsilon)_{\mathrm{AGX}}$, see Eq. (7). $\mathrm{tr}\,(\varepsilon)_{\mathrm{CG}}$ and $\mathrm{tr}\,(\varepsilon)_{\mathrm{AGX}}$ are plotted in Fig. 39. By assuming that $\mathrm{tr}\,(\varepsilon)_{\mathrm{AGX}}$ is the true volume strain, we compute estimated absolute and relative errors for $\mathrm{tr}\,(\varepsilon)_{\mathrm{CG}}$, see Figs. 40 and 41.
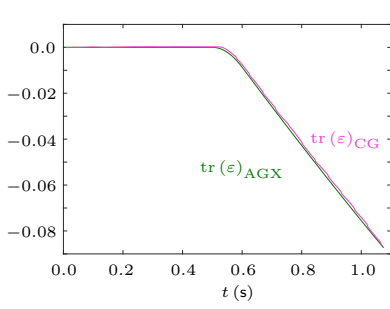
Figure 39 – $\text{tr}\,(\varepsilon)_{\text{AGX}}$ and $\text{tr}\,(\varepsilon)_{\text{CG}}$.
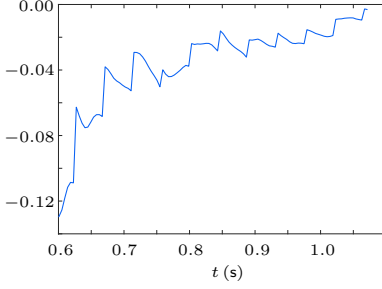
Figure 40 – Estimated relative error ϵ_{rel} for $\text{tr}\,(\varepsilon)$.
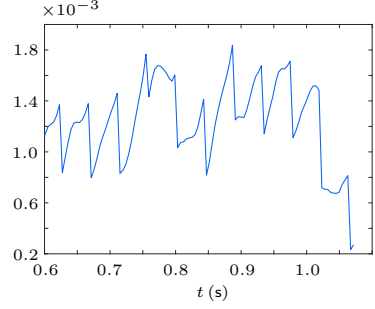
Figure 41 – Estimated absolute error ϵ_{abs} for $\text{tr}\,(\varepsilon)$.
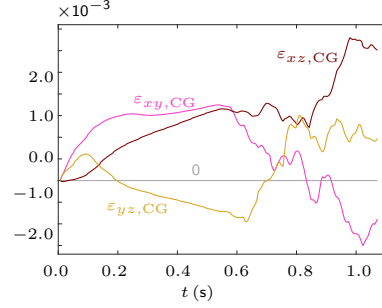
As before, we take the average of the magnitude of the relative error at $t > 0.6$ and obtain[*]

$$\bar{\epsilon}_{\text{rel}}\left(\text{tr}\,(\varepsilon)_{\text{CG}}\right) = 0.036 \pm 0.026, \qquad 0.6 \text{ s} < t.$$

We note that $\text{tr}\,(\varepsilon)_{\text{AGX}}$ follows $\text{tr}\,(\varepsilon)_{\text{CG}}$ very closely. Moreover, the relative error is small.

Plots for the average of σ_{xy}, σ_{xz} and σ_{yz} are given in Fig. 42.

Results for the mean normal strain rate, i.e. $\text{tr}\,(\dot{\varepsilon})\,/3$, are given in Fig. 43.

Figure 42 – Components $\varepsilon_{ij,\text{CG}}$ with a reference line at 0.

---

[*]At $t < 0.5$ s, $(\Delta V / V)_{\text{AGX}} = 0$ since the walls were held static during that time (yielding an infinite relative error). Moreover, at 0.5 s $< t < 0.6$ s, both $(\Delta V / V)_{\text{AGX}}$ and $\text{tr}\,(\varepsilon)_{\text{CG}}$ are very small, yielding a large, ambiguous relative error. Hence we settle for the average at $t > 0.6$ s.
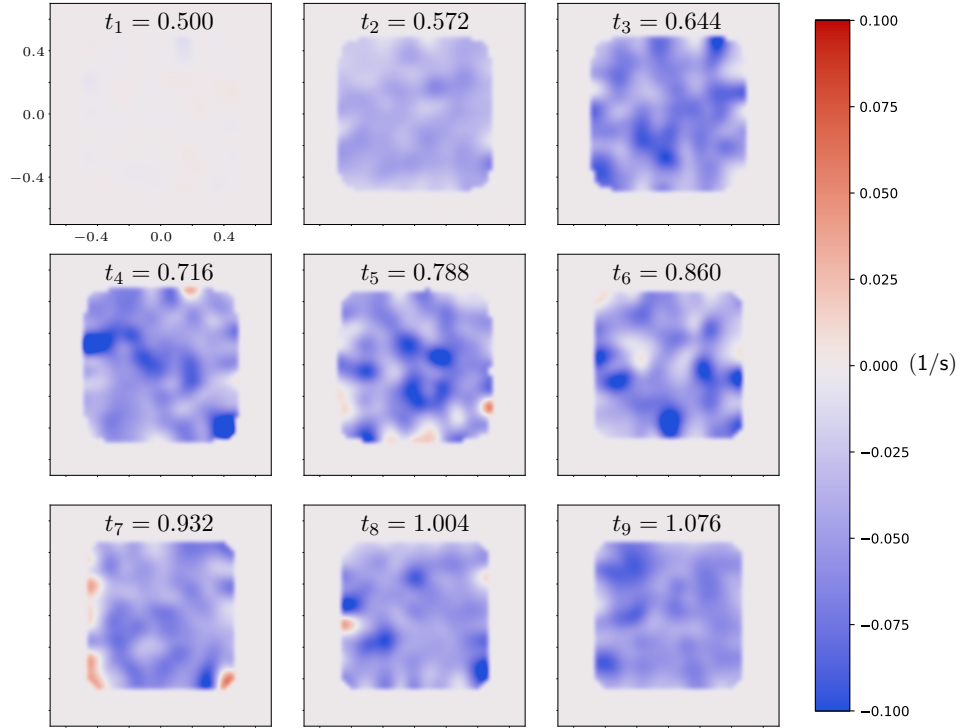
Figure 43 – The mean normal strain rate, i.e. $\mathrm{tr}\,(\dot{\varepsilon})\,/3$, at regular time intervals (s), from $t = 0.5$ s to the end of the test. Horizontal axis is x (m), vertical axis is z (m). Notice the small regions near the boundaries with positive strain rates.

We let $\mathrm{tr}\,(\dot{\varepsilon})_{\mathrm{CG}}$ denote the average of $\mathrm{tr}\,(\dot{\varepsilon})$, based on the numerical CG data. We let the estimated function for $\mathrm{tr}\,(\dot{\varepsilon})$ be denoted $\mathrm{tr}\,(\dot{\varepsilon})_{\mathrm{AGX}}$ (for its derivation, see the Appendix, Section A.4.2). $\mathrm{tr}\,(\dot{\varepsilon})_{\mathrm{AGX}}$ and $\mathrm{tr}\,(\dot{\varepsilon})_{\mathrm{CG}}$ are compared in Fig. 44. We assume that $\mathrm{tr}\,(\dot{\varepsilon})_{\mathrm{AGX}}$ is the true function, and thereby estimate relative and absolute errors for $\mathrm{tr}\,(\dot{\varepsilon})_{\mathrm{CG}}$, see Figs. 45 and 46.
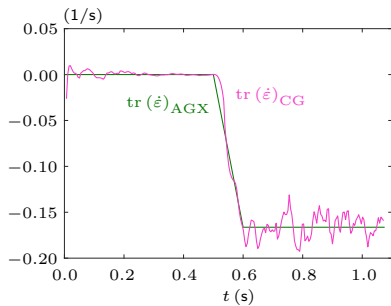
Figure 44 – $\mathrm{tr}\,(\dot{\varepsilon})_{\mathrm{AGX}}$ and $\mathrm{tr}\,(\dot{\varepsilon})_{\mathrm{CG}}$.
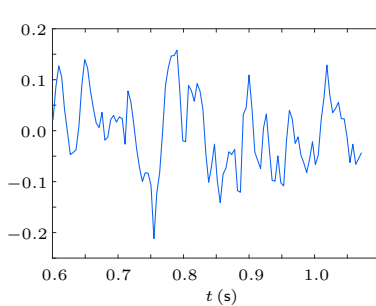
Figure 45 – Estimated relative error $\epsilon_{\mathrm{rel}}\,(\mathrm{tr}\,(\dot{\varepsilon})_{\mathrm{CG}})$ for $\mathrm{tr}\,(\dot{\varepsilon})_{\mathrm{CG}}$.
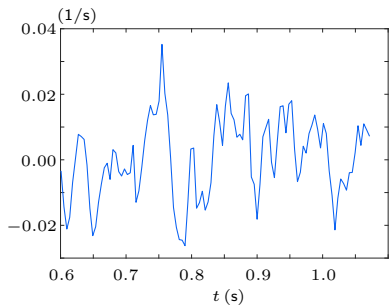
Figure 46 – Estimated absolute error $\epsilon_{\mathrm{abs}}\,(\mathrm{tr}\,(\dot{\varepsilon})_{\mathrm{CG}})$ for $\mathrm{tr}\,(\dot{\varepsilon})_{\mathrm{CG}}$.

We take the average of the magnitude of the relative errors at $t > 0.6$ s and obtain

$$\bar{\epsilon}_{\text{rel}} \left(\text{tr} \left(\dot{\varepsilon} \right)_{\text{CG}} \right) = 0.062 \pm 0.074, \qquad 0.6 \text{ s} < t.$$

We note that $\text{tr} \left(\dot{\varepsilon} \right)_{\text{CG}}$ agrees quite well with $\text{tr} \left(\dot{\varepsilon} \right)_{\text{ana}}$, although, at $t > 0.6$ s, there are substantial fluctuations. These fluctuations seems to be centered roughly around the analytical value. The red regions near the boundaries in Fig. 43 may be due to boundary effects. Another possible reason is that the conditions for the particles near a wall are different than in the bulk—particles near a wall are in contact with both the wall and particles, while particles in the bulk are in contact only with particles.

The results for the power density are given in Fig. 47.
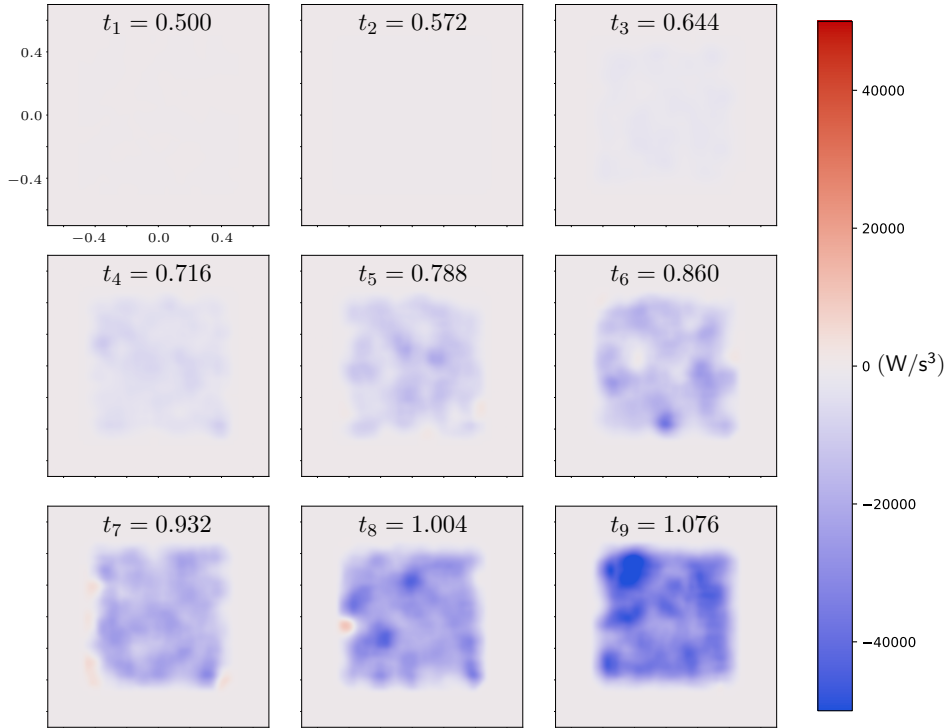
Figure 47 – The power density at regular time intervals (s), from $t = 0.5$ s to the end of the test. Horizontal axis is x (m), vertical axis is z (m).

We let S_{CG} denote the average of the power density as a function of time, based on the numerical CG data. By consulting the data produced by AGX, we constructed the function S_{AGX} (for its derivation see the Appendix, Section A.4.3). S_{AGX} and S_{CG} are compared in Fig. 48. We assume that S_{AGX} is the true power density and calculate relative and absolute errors for S_{CG}, see Figs. 49 and 50.
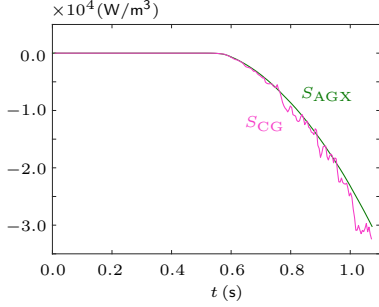
Figure 48 – Power densities S_{AGX} and S_{CG}.
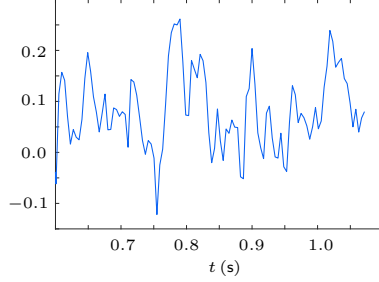
Figure 49 – Estimated relative error $\epsilon_{\mathrm{rel}}(S_{\mathrm{CG}})$ for S_{CG}.
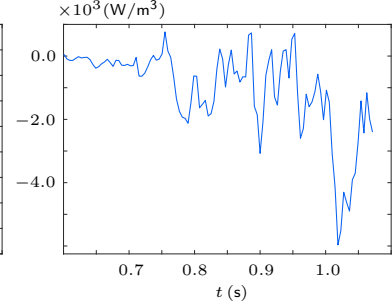
Figure 50 – Estimated absolute error $\epsilon_{\mathrm{rel}}(S_{\mathrm{CG}})$ for S_{CG}.

The average of the magnitude of the relative error is

$$\bar{\epsilon}_{\mathrm{rel}}(S_{\mathrm{CG}}) = 0.090 \pm 0.075, \qquad 0.6\text{ s} < t.$$

We see that S_{CG} agree quite well with S_{AGX}, although there are some fluctuations. Moreover, S_{CG} seems most often to yield a larger magnitude than S_{AGX}.

4.2 Deviations from Analytical or Expected Results

All analytical and expected results were based on the assumption that the particles were distributed evenly in the sample. This was not the case, see the Appendix, Section A.4.4. Also, the solids were composed of a finite number of particles, so the dynamics over a region no larger than the sample itself were not perfectly uniform due to granularity. This yielded non-uniform displacement. These two factors obviously introduced deviations. Quite large deviations are seen in the velocity plots. It is not unreasonable that strong normal force chains built up during a test. As these chains broke, the result was unpredictable velocities. Also, for example, displacement—which carried a smaller relative error than velocity—is measured against a reference configuration (perhaps a thousand timesteps prior), while velocity is measured against the configuration one timestep prior. This makes velocity more prone to exhibit fluctuations. However, for the isotropic test with particles in perfect cubic formation, see the Appendix, Section A.4.5, the experimental velocity agrees very well with the analytical velocity, indicating that the CG plots reflect true behaviour.

The *analytical* off-diagonal components σ_{ij} $(i \neq j)$ and ε_{ij} $(i \neq j)$ are zero for the isotropic compression test, while they are *experimentally* non-zero. Consider the strain tensor. If, for example, the strain in x-direction is dependent on y or z, then by Eq. (6), non-zero off-diagonal components are yielded. Given the random configuration of the particles, and the inhomogeneity described above, it is not improbable that this dependency existed in some places. Moreover, for the isotropic test with particles in cubic formation, σ_{ij} $(i \neq j)$ and ε_{ij} $(i \neq j)$ are zero, as expected, indicating again that the CG plots reflect true behaviour.

There were also errors introduced by the size of the timestep and the number of iterations. However, these parameters were set so that numerical errors should be around 0.01, so these parameters were not likely to be the major source of the deviations.

The implemented strain tensor is of first order. The compression was 3% for the isotropic test, with good results for ε_{ij} $(i = j)$, indicating that compressions of at least 3% is unproblematic. Thus, the strain tensor being of first order is unlikely to be a major source of errors. Moreover, for the triaxial test, see the Appendix, Section A.4.8, ε_{zz} agrees very well with expected behaviour, and the compression was 10% in the z-direction in that test.
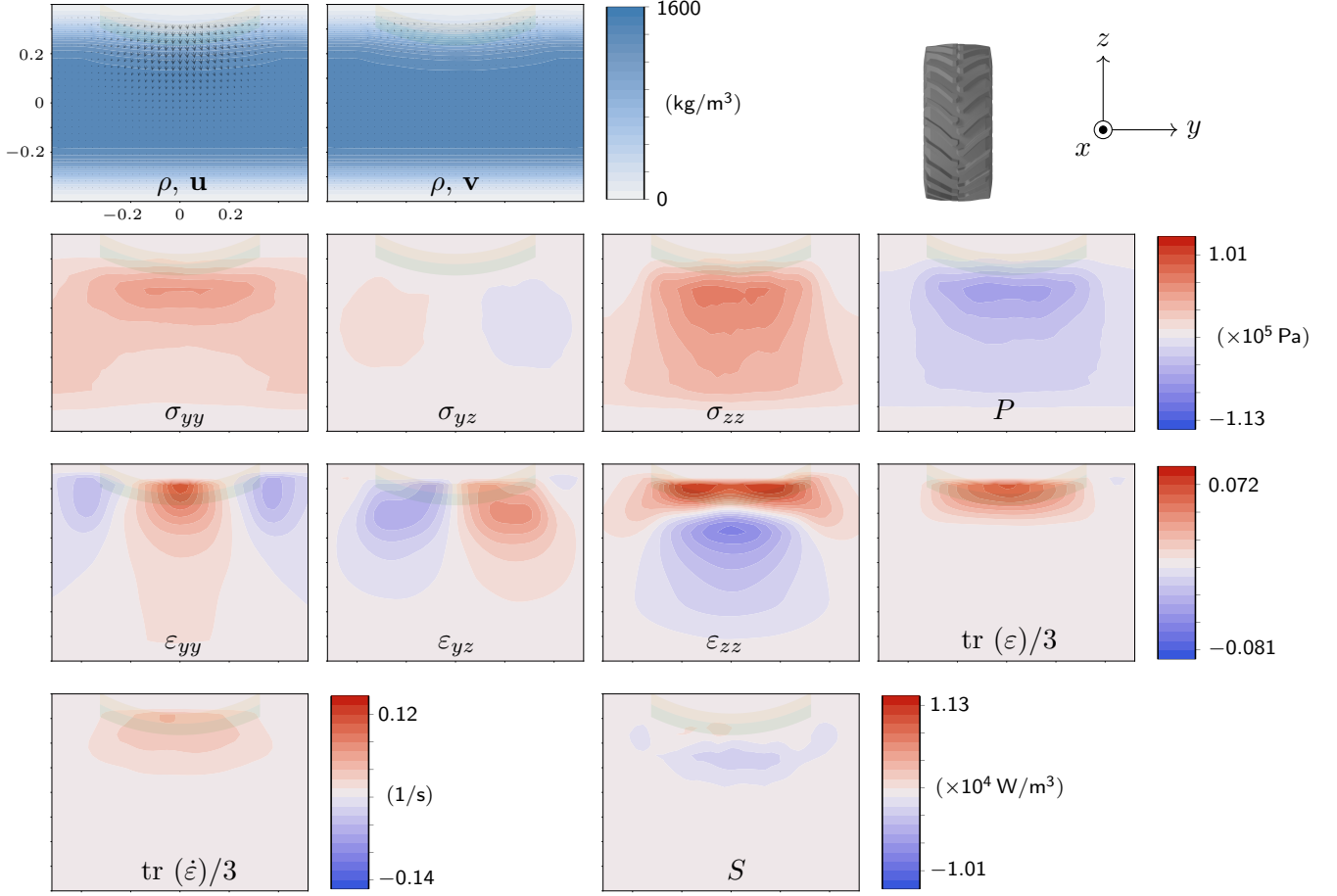
4.3 Vehicle on Soil

The results for the vehicle on soil in the xz-plane are given in Fig. 51. In this section, contour lines are used consistently for the scalar fields. See Table 3 for technical details, such as particle radii, values for Young moduli, etc.
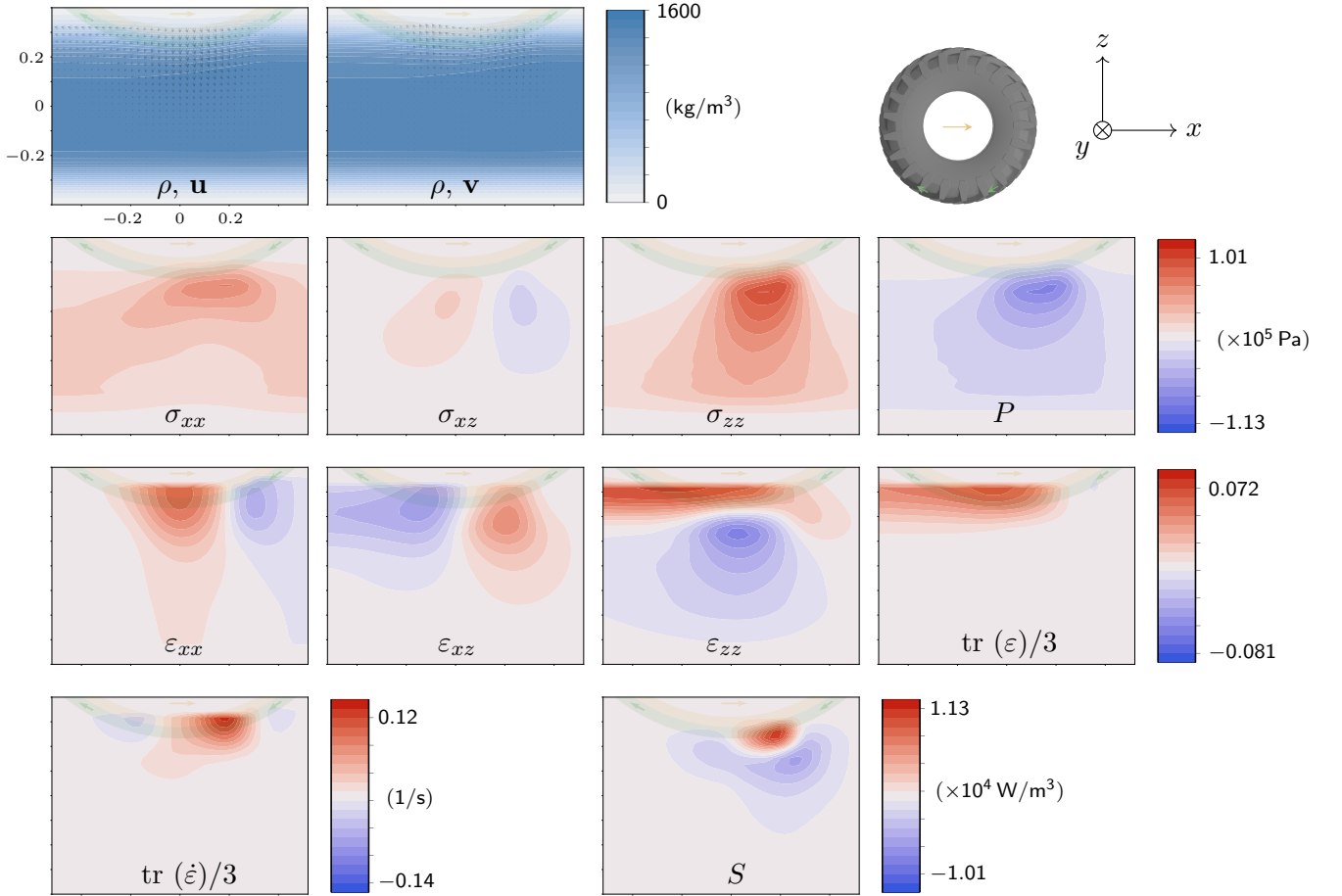
Figure 51 – Selected time-averaged quantities in the xz-plane $(y = 0)$ for the vehicle on soil. See Table 1 for variable explanations. The transparent green band indicates the thread, and the transparent yellow band indicates the part of the tyre (with varying radius) to which the thread is attached. Horizontal axis is x (m), vertical axis is z (m).

The results for the vehicle on soil in the yz-plane are given in Fig. 52.

Figure 52 – Selected time-averaged quantities in the yz-plane ($x = 0$) for the vehicle on soil. The vehicle moves out of the screen. See Table 1 for variable explanations. The transparent green band indicates the thread, and the transparent yellow band indicates the part of the tyre (with varying radius) to which the thread is attached. Horizontal axis is y (m), vertical axis is z (m).

Magnifications for ρ, **u** in Figs. 51 and 52 are given in the Appendix, Section A.4.10.

By studying the mass density ρ in Fig. 51, we note that the density is lower to the left of the tyre than in front of it. Moreover, the same field in Fig. 52 indicates a lower density under the tyre than to the left and right of it. This indicates that the soil expanded under the tyre. Volume expansion is often a result of shearing, see Fig. 4, so we expect ε_{xz} in Fig. 51 to be non-zero, which is also the case.

In [30] the authors analyzed the stress in a DEM-soil under a heavy vehicle and produced experimental plots. The general behaviour of
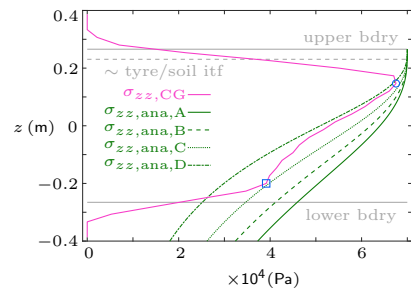
Figure 53 – $\sigma_{zz,\mathrm{CG}}$ and $\sigma_{zz,\mathrm{ana}}$. The capital letters refer to different contact areas of the tyre: $\{A, B, C, D\} = \{0.29, 0.23, 0.16, 0.10\}$ m^2. The estimated contact area is B. The interval between the blue circle and square is considered to be devoid of boundary effects.

their plots agree quite well with σ_{xx} and σ_{zz} in Fig. 51.

In both Fig. 51 and 52, the volume strain $\mathrm{tr}\,(\varepsilon)$ indicates expansion near the tyre-soil interface. This might reflect particle detachment from the surface of the soil due to the tyre, but this is near a boundary, where plots are unreliable. In both figures, down in the soil, ε_{zz} indicates compression in the z-direction, which is expected. Also, in both figures the power density S indicates that, down in the soil, energy was transferred to the soil, while at the surface (near the boundary) energy was released from the soil. The energy transfer to the soil is expected, since compression increases the amount of elastically stored energy.

We conclude by comparing σ_{zz} in Fig. 52 with the analytical σ_{zz} for a linear elastic solid, see Eq. (2.3.11), which we denote $\sigma_{zz,\mathrm{ana}}$. We let $\sigma_{zz,\mathrm{CG}}{}^{*}$ denote the value at z, based on the CG data. $\sigma_{zz,\mathrm{ana}}$ and $\sigma_{zz,\mathrm{CG}}$ are plotted in Fig. 53. In this figure, the distance from the blue circle to the estimated tyre-soil interface is $4.8r$, where r is the average particle radius. The distance from the blue square to the lower boundary is $3.7r$. The general agreement between $\sigma_{zz,\mathrm{ana}}$ and $\sigma_{zz,\mathrm{CG}}$ is decent, but far from perfect. This is expected due to a number of reasons. Firstly, $\sigma_{zz,\mathrm{ana}}$ is valid for an elastic solid, while the soil was elastoplastic. Secondly, $\sigma_{zz,\mathrm{ana}}$ is valid for a stationary circular plate, while a rotating tyre stressed the soil. Thirdly, $\sigma_{zz,\mathrm{ana}}$ assumes a half-space (of infinite depth), while the soil had a finite depth.

5 Summary and Conclusions

In summary, the CG plotting technique offers a powerful and useful tool for investigating the dynamics of soil. The system of plots offers quick analysis. The general behaviour of most plots agreed well with expected behaviour. Relative errors ranged from 1.2 to 27%. Fields that are considered to agree best with expected behaviour are mass density, displacement, pressure, and volume strain (the trace of the strain tensor). For most parts, these fields also carried small relative errors in the tests. In particular, the pressure was tested quite extensively. Its behaviour with respect to isotropic compression, increasing/decreasing pressure (the evolution of the pressure during the gravity test), and hydrostatic pressure agreed very well with expected result. Individual components of the stress and strain tensors agreed less well with expected results, but this was not entirely unexpected due to particle fluctuations in the sample. Such fluctuations are mitigated by taking the trace of the tensors. Moreover, the non-diagonal components for the stress and strain tensors were consistently zero for the tests with particles in cubic formation, as expected. A short analysis was performed for the non-diagonal components of the strain tensor in which the expected result was non-zero. The behaviour agreed well with expected behaviour, although its relative error was quite high.

The greatest disadvantage with the technique was found to be the unreliability near the boundaries. This was not unexpected due to the technical averaging nature of the CG. However, it is disadvantageous, since the behaviour of the soil at the contact between the soil and the tyre is of interest. Based on the tests, the results are unreliable within a distance of $2.7r$ from a boundary, where r is the average particle diameter. However, based on the results from the vehicle on soil, the same distance is $3.7r$ or $4.8r$ although

---

*the average is taken over four voxels in the y-direction, centered about the tyre.

that analysis was based partially on the assumption that the soil is linearly elastic (which it is not). Boundary effects can be managed by adding correction terms, and a complete CG treatment should include such terms.

The phenomenon of compaction or expansion can be studied by analyzing the mass density or trace of the strain tensor. It is not recommended to use bicubic interpolation and a small interval for the mass density since this introduces strong boundary effects. However, by using a large interval and contour lines, compaction or expansion can be revealed successfully.

For vehicle-soil dynamics, time averaging is recommended to mitigate fluctuations in the fields. Also, for such averaging, it is advised to use only plots in which local soil conditions are unchanged, and discard plots in which e.g. the vehicle is near a boundary.

Also, for the vehicle on soil, the results for σ_{xx} and σ_{zz} in Fig. 51 agreed quite well with the experimental results from the authors of [30]. Moreover, the behaviour of σ_{zz} agreed quite well with the analytic behaviour of σ_{zz} in an elastic solid, indicating that the stress in the soil can be crudely approximated as the stress in a linear elastic solid. However, it is far from a perfect match. This is also expected, since, among other things, a soil is elasto-plastic, while the analytical function assumes an elastic solid.

In Table 1, a summary of the results from the tests is given.

Table 1 – Summary of the results for the tests. The adjectives describe the agreement between the general behaviour of the plot and the analytical/expected general behaviour. In descending order for the grade, the adjectives are: "excellent", "very good", "good","okay", and "poor". The numbers refer to the average of the magnitude of the relative errors.

	Iso, R	Iso, C	Grav, R	Grav, C	Triax, R	Shear, R
ρ	excellent 4.9%					
u_i	very good 2.5%	excellent 2.9%	very good	excellent 2.1%	very good	good
$\mathbf{u}$	good	excellent	very good	excellent	very good	good
v_i	okay 12%	excellent 1.2%				
$\mathbf{v}$	okay	excellent				
P	very good 8.5%		very good 6.5, 5.9%			
σ_{ii}	very good		very good			
σ_{ij}	good	excellent	very good	excellent		
$\mathrm{tr}\,\varepsilon$	excellent 3.6%	good	good	excellent	good	good
ε_{ii}	good	good	poor	excellent	very good 25, 7.3, 2.1%	poor
ε_{ij}	okay	excellent	poor	excellent	good	okay 27%
$\dot{\varepsilon}_{ii}$	very good 6.2%		good			
S	good 9.0%		good			

Iso	isotropic compression test	**Shear**	simple shear test	$\mathbf{v}$	velocity vector	ε_{ii}	normal strain tensor components
R	random configuration	ρ	mass density	P	pressure	ε_{ij}	shear strain tensor components
C	cubic formation	u_i	displacement component i	σ_{ii}	normal stress tensor components	$\dot{\varepsilon}_{ii}$	time derivative of ε_{ii}
Grav	gravitational test	$\mathbf{u}$	displacement vector	σ_{ij}	shear stress tensor components	S	power density
Triax	triaxial test	v_i	velocity component i	$\mathrm{tr}\,\varepsilon$	trace of strain tensor		

6   Acknowledgements

7   References

References

[1] A. Verruijt. An Introduction to Soil Mechanics. Theory and Applications of Transport in Porous Media, Vol. 30. Springer International Publishing AG (2018), p. 4.

[2] Ibid, pp. 4-6.

[3] Ibid, Fig. 12.3, p. 99.

[4] Ibid, p. 110.

[5] Ibid, p. 173.

[6] Ibid, p. 225.

[7] A. Ziyaee, M. R. Roshani. A survey study on Soil compaction problems for new methods in agriculture. Int. Res. J. Appl. Basic Sci. 3 (9), 1787, 2012.

[8] V. Wiberg, M. Servin and T. Nordfjell. Numerical soil under heavy vehicles. Submitted manuscript (2019).

[9] C. Coetzee, Review: Calibration of the discrete element method, Powder Technology 310 (2017) pp. 104—142.

[10] S. Luding. Introduction to Discrete Element Method. European Journal of Environmental and Civil Engineering, 12(7-8):785—826 (2008), p.4.

[11] M. Servin. Simulation models of terrain and machines (2019).

[12] J. N. Reddy. An Introduction to Continuum Mechanics, 2nd Edition, Cambridge University Press (2013), p.1.

[13] Ibid, p. 82.

[14] Ibid, p. 83.

[15] Ibid, p. 89.

[16] Ibid, p. 104.

[17] Ibid, p. 154.

[18] Ibid, p. 180.

[19] K. L. Johnson, Contact Mechanics, Cambridge University Press, 1985.

[20] I. Goldhirsch. Stress, stress asymmetry and couple stress: from discrete particles to continuous fields. Granular Matter 2010; 12(3):239–252.

[21] D. R. Tunuguntla, A. R. Thornton and T. Weinhart. Discrete particles to continuum fields: Coarse-Graining, An accurate micro-macro mapping technique. Multi-Scale Mechanics Group, University of Twente, Enschede, The Netherlands. 20XX.

[22] J. Zhang, R. P. Behringer, and I. Goldhirsch. Coarse-Graining of a Physical Granular System. Progress of Theoretical Physics Supplement, 184:16—30, 03 2010.

[23] J. Titus, S. Geroge. A Comparison Study On Different Interpolation Methods Based On Satellite Images. Viswajyothi College of Engineering and Technology, Muvattupuzha, Kerala, India.

[24] AGX Dynamics, Algoryx. API Programming Course (201X), p. 9.

[25] Ibid, p.10.

[26] M. Servin, D. Wang, C. Lacoursière, and K. Bodin. Examining the smooth and nonsmooth discrete element approaches to granular matter. International Journal for Numerical Methods in Engineering, vol 97, no. 12, 878–902 (2014).

[27] M. Abramowitz and I. A. Stegun (Eds.). Handbook of Mathematical Functions with Formulas, Graphs, and Mathematical Tables, 10th printing. New York: Dover (1972), p. 14.

[28] W. Benenson et al (Eds.). Handbook of Physics, Vol. 1. Springer-Verlag New York (2002), p. 174.

[29] T. Weinhart, A.R. Thornton, S. Luding, O. Bokhove. From discrete particles to continuum fields near a boundary. Granular Matter, 14 (2012).

[30] J. De Pue, W. M. Cornelis. DEM simulation of stress transmission under agricultural traffic Part 1: Comparison with continuum model and parametric study, Soil Tillage Res., 195 (2019).

A   Appendix

A.1   Analytical Solutions: Displacement, Velocity, Strain Tensor and Volume Strain

The displacement vector fields for the deformations in Figs. 11, 12, 13 and 14 are

$$
\mathbf{u} =
\begin{cases}
\dfrac{\Delta L}{L} \dfrac{t}{t_{\text{end}}} \left(x, y, z\right), & \text{(isotropic compression)} & \text{(11a)} \\[2ex]
\dfrac{t}{t_{\text{end}}} \left(\dfrac{\Delta L_x}{L} x, \dfrac{\Delta L_y}{L} y, \dfrac{\Delta L_z}{L} z\right), & \text{(triaxial test)} & \text{(11b)} \\[2ex]
\left(\dfrac{L}{2} \tan\left(\dfrac{t}{t_{\text{end}}}\theta\right) z, 0, 0\right), & \text{(simple shear)} & \text{(11c)} \\[2ex]
\left(0, 0, \dfrac{t}{t_{\text{end}}} \left[K_1 z + K_2\right]\right), & \text{(gravitational compression)} & \text{(11d)}
\end{cases}
$$

where

$$
\begin{cases}
\mathbf{u} \equiv \left(u_x, u_y, u_z\right), \\
\Delta L/L \equiv (L' - L)/L, \\
\Delta L_x/L \equiv (L'_x - L)/L, \\
\Delta L_z/L \equiv (L'_z - L)/L, \\
K_1, K_2 > 0.
\end{cases}
$$

The velocity displacement fields are, by Eq. (1) and $\mathbf{u} \equiv \mathbf{x} - \mathbf{X}$, where $\mathbf{X}$ is independent of time:

$$
\mathbf{v} =
\begin{cases}
\dfrac{\Delta L}{L} \dfrac{1}{t_{\text{end}}} \left(x, y, z\right), & \text{(isotropic compression)} & \text{(12a)} \\[2ex]
\dfrac{1}{t_{\text{end}}} \left(\dfrac{\Delta L_x}{L} x, \dfrac{\Delta L_y}{L} y, \dfrac{\Delta L_z}{L} z\right), & \text{(triaxial test)} & \text{(12b)} \\[2ex]
\left(\dfrac{L}{2} \dfrac{\theta}{t_{\text{end}}} \sec^2\left(\dfrac{t}{t_{\text{end}}}\theta\right) z, 0, 0\right), & \text{(simple shear)} & \text{(12c)} \\[2ex]
\left(0, 0, \dfrac{K_1}{t_{\text{end}}} z\right). & \text{(gravitational compression)} & \text{(12d)}
\end{cases}
$$

By Eq. (6), the linear strain tensors are

$$
\mathbf{e} = \begin{cases}
\dfrac{\Delta L}{L}\dfrac{t}{t_{\text{end}}}\begin{pmatrix} 1 & 0 & 0 \\ 0 & 1 & 0 \\ 0 & 0 & 1 \end{pmatrix}, & \text{(isotropic compression)} & \text{(13a)} \\[20pt]
\dfrac{t}{t_{\text{end}}}\begin{pmatrix} \Delta L_x/L & 0 & 0 \\ 0 & \Delta L_y/L & 0 \\ 0 & 0 & \Delta L_z/L \end{pmatrix}, & \text{(triaxial test)} & \text{(13b)} \\[20pt]
\dfrac{L}{2}\tan\left(\dfrac{t}{t_{\text{end}}}\theta\right)\begin{pmatrix} 0 & 0 & 1 \\ 0 & 0 & 0 \\ 1 & 0 & 0 \end{pmatrix}, & \text{(simple shear)} & \text{(13c)} \\[20pt]
K_1\dfrac{t}{t_{\text{end}}}\begin{pmatrix} 0 & 0 & 0 \\ 0 & 0 & 0 \\ 0 & 0 & 1 \end{pmatrix}. & \text{(gravitational compression)} & \text{(13d)}
\end{cases}
$$

By Eq. (7), the volume strains are

$$
\frac{\Delta V}{V} = \begin{cases}
3\dfrac{\Delta L}{L}\dfrac{t}{t_{\text{end}}}, & \text{(isotropic compression)} & \text{(14a)} \\[16pt]
\dfrac{t}{t_{\text{end}}}\left(\dfrac{\Delta L_x}{L} + \dfrac{\Delta L_y}{L} + \dfrac{\Delta L_z}{L}\right), & \text{(triaxial test)} & \text{(14b)} \\[16pt]
0, & \text{(simple shear)} & \text{(14c)} \\[16pt]
K_1\dfrac{t}{t_{\text{end}}}. & \text{(gravitational compression)} & \text{(14d)}
\end{cases}
$$

A.2   Details for Test Sample Creation

For the test sample in Fig. 17, the particles were simply placed in a primitive cubic formation such that the inner surfaces of the six walls just grazed the layers of particles that were nearest the walls.

For the test sample in Fig. 18, the particles were spawned at random locations within the walls during 0.5 s (such that the number of particles increased with time). Particles were spawned with zero velocity, but they collided with each other during the creation, giving them small velocities. After all particles had spawned, a relaxation time of 0.5 s followed during which the particles distributed themselves more evenly. After the relaxation time, all walls were driven towards the origin with motors. The left and right walls were constrained to have only translational motion along the x-axis. Similarly, the back and front walls moved along the y-axis, and the top and bottom walls moved along the z-axis. Consequently, the right angles between the walls were maintained. The target velocity for the walls was 2.5 cm/s, but the *set* maximum force of the motors was such that the pressure at the walls could not exceed 1.0 kPa (more precisely, the force applied on wall i was at maximum 1.0 kPa times the side area of the sample in contact with wall i). Thus, as the walls moved inwards, the pressure inside the sample increased,

and the motors needed to apply greater and greater forces. When the pressure reached 1.0 kPa, the walls were no longer allowed to compress the sample further. When the *actual* forces applied by the motors (as determined by AGX) were such that the pressure was within 5% of 1.0 kPA for 250 timesteps, the state of the particles was saved into a test sample with an internal pressure 1.0 kPa.

Table 2 – Parameters for the creation of the test samples, and for the tests.

Parameter	Applies to Fig. 17?	Applies to Fig. 18?	Value
Timestep (simulation)	✓	✓	$1/2500$ s
No. iterations (simulation)	✓	✓	500
Particle mass density	✓	✓	2×10^3 kg/m^3
Wall mass density	✓	✓	10^4 kg/m^3
Particle radius	✓		2 cm
Particle radii		✓	$(2, 1.7, 1.2)$ cm
Mass contribution†		✓	$(0.5, 0.3, 0.2)$
Young Modulus (particle)	✓	✓	10^8 Pa
Young Modulus (wall)	✓	✓	10^{11} Pa
Friction coefficient	✓	✓	0
Rolling resistance	✓	✓	0 N
Cohesion	✓	✓	0
Cohesive overlap	✓	✓	0.1 cm
Sample pressure		✓	1.0×10^3 Pa

† Normalized contribution to total sample mass by particle radii (in same order as radii are given)

A.3 Details for Vehicle on Soil

Table 3 – Parameters for the vehicle on soil.

Parameter	Value
Timestep (simulation)	$0.0003 \approx 1/3333$ s
No. iterations (simulation)	1500
Particle mass density	2×10^3 kg/m^3
Wall mass density	10^4 kg/m^3
Particle radii	$(2, 1.7, 1.2)$ cm
Mass contribution†	$(0.5, 0.3, 0.2)$
Young Modulus (particle)	10^8 Pa
Young Modulus (wall)	10^{11} Pa
Young Modulus (tyre)	10^{11} Pa
Friction coefficient (particle)	0.15
Friction coefficient (tyre)	0.6
Rolling resistance	0.025 N
Cohesion	20
Cohesive overlap	0.001 cm
Total vehicle mass	3600 kg
Outer Tyre Radius	0.75 m
Tire tread depth	~ 5 cm
Sample pressure	1.0×10^5 Pa

† Normalized contribution to total sample mass by particle radii (in same order as radii are given)

A.4 Results

A.4.1 Isotropic Compression—Random Configuration: Derivation of $P_{\mathbf{AGX}}$

As the sample got increasingly compressed, the pressure within the sample increased. In order for the walls to continue to compress the sample, greater and greater forces had to be exerted on them. This increased the pressure at the surfaces of the sample, which, by diffusion, should equal the pressure inside the sample—particularly at high pressure when forces are readily transmitted between the particles. To obtain the pressure inside the sample, we stored the applied forces by the virtual AGX motors at each timestep, and also the sample dimensions. We define P_{AGX} as the sum of all motor forces divided by the total surface area of the sample. Now, as the walls accelerated, parts of the motor forces were devoted to overcome the inertia of the walls, but at 0.6 s the final constant speed was reached, i.e. at $t > 0.6$ s, the motor forces were dedicated to only compress the sample so then P_{AGX} should have been equal to the pressure within the sample.

A.4.2 Isotropic Compression—Random Configuration: Derivation of $\mathrm{tr}\,(\dot{\varepsilon})$

We have

$$\mathrm{tr}\,(\varepsilon)_{\text{AGX}} = \int_0^{t_{\text{end}}} \mathrm{tr}\,(\dot{\varepsilon})_{\text{est}}\, dt,$$

43

where $\mathrm{tr}\,(\varepsilon)_{\mathrm{AGX}}$ is the experimental volume strain provided by the AGX software (same quantity as in Fig. 39). Now, the walls moved with the following speed

$$
v_{\mathrm{walls}} = \begin{cases} 0, & 0 < t < 0.5 \text{ s,} \\ k(t-0.5) & 0.5 \text{ s} < t < 0.6 \text{ s,} \\ 0.1k & 0.6 \text{ s} < t < t_{\mathrm{end}}, \end{cases}
$$

where k is a real constant such that $v_{\mathrm{walls}} = 2.5$ cm/s at $t > 0.6$ s. Then, since the time derivative of the volume strain is linearly proportional to the speed of the walls, we have

$$
\mathrm{tr}\,(\dot{\varepsilon})_{\mathrm{est}} = \begin{cases} 0, & 0 < t < 0.5 \text{ s,} \\ K(t-0.5) & 0.5 \text{ s} < t < 0.6 \text{ s,} \\ 0.1K & 0.6 \text{ s} < t < t_{\mathrm{end}}. \end{cases}
$$

where K is some real constant. To find $\mathrm{tr}\,(\dot{\varepsilon})_{\mathrm{est}}$, it remains to determine K, which is done by integrating $\mathrm{tr}\,(\dot{\varepsilon})_{\mathrm{esta}}$:

$$
\mathrm{tr}\,(\varepsilon)_{\mathrm{AGX}} = 0 \int_0^{0.5} dt + K \int_{0.5}^{0.6} (t-0.5)\,dt + 0.1K \int_{0.6}^{t_{\mathrm{end}}} dt.
$$

A.4.3 Isotropic Compression—Random Configuration: Derivation of S_{AGX}

We let the force applied by each of the six motors that moved the walls be denoted $F_{i,\mathrm{motor}}(t) > 0$, $i = 1, \ldots 6$, and the distance each wall travelled during one time step be denoted $\Delta L_i(t)$. Then, the energy spent by each motor each time step was $F_{i,\mathrm{motor}}(t)\Delta L_i(i)$. All of this energy went into the sample as elastically stored energy, except for the increase in kinetic energy in the walls. We let the increase in kinetic energy for each wall during one time step be denoted $\Delta E_{i,\mathrm{kin}}(t)$. Then, each wall contributed during one time step with the energy $F_{i,\mathrm{motor}}(t)\Delta L_i(t) - \Delta E_{i,\mathrm{kin}}(t)$ to the sample. By summing the contributions from each motor, dividing by the volume $V(t)$ of the sample, dividing by the time step Δt, and supplying a minus sign, we obtain the expected power density for the test:

$$
S_{\mathrm{AGX}}(t) = \frac{1}{V(t)\Delta t} \sum_{i=1}^{6} \left[F_{i,\mathrm{motor}}(t)\Delta L_i(t) - \Delta E_{i,\mathrm{kin}}(t) \right].
$$

A.4.4 Uneven Particle Distribution in Sample

By selecting a small interval for the mass density that is centered around the average density, the sample near the boundaries disappear from the plot due to the averaging nature of the CG, see Fig. 54. For example, for a voxel centered at a point on the boundary, half of the volume of the voxel resides inside the sample, where particles contribute to the density. Half of the volume of the voxel, however, resides in empty space, reducing the value of
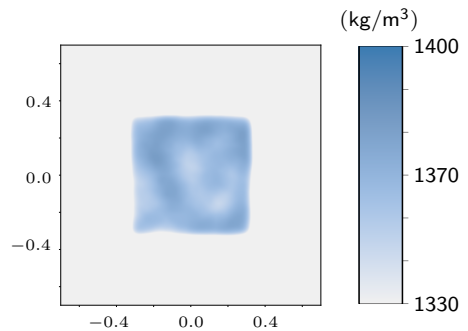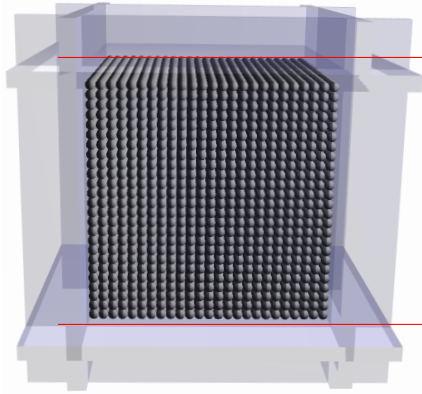
**Figure 54** – Mass density at $t = 0.004$ s, i.e. at the start of a test (random configuration).

the density. Also, we note that the density is not
uniform, neither at the boundaries nor within the
sample.

A.4.5 Isotropic Compression Test—Particles in Simple Cubic Formation

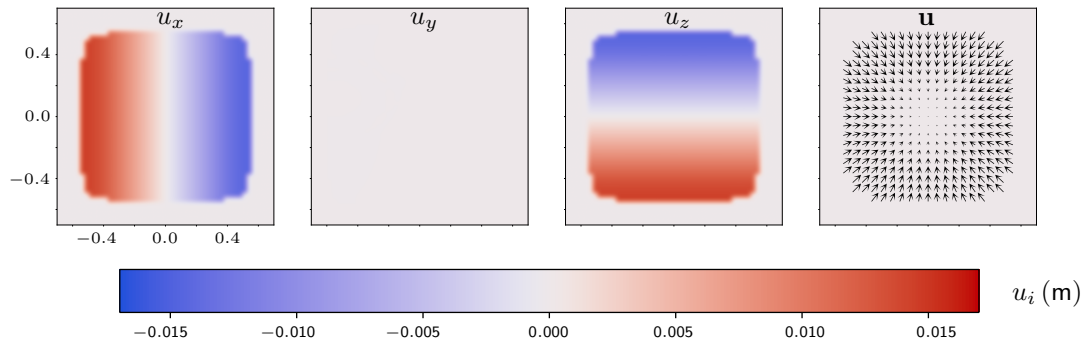This is the same test as in Section 4.1.1, but here the test sample in Fig. 17 was used.

**Figure 55** – The test sample at $t = 0$ s (same as Fig. 17).
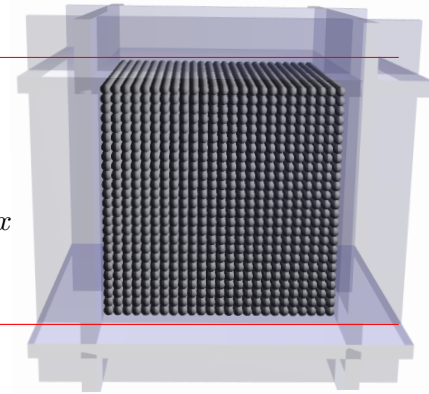
Figure 56 – The test sample at $t = 1.148$ s, when the compression is complete. Note that the simple cubic formation is retained.

In Fig. 57, the results for the displacement **u** and its components are shown.

Figure 57 – The displacement **u** and its components at $t = 1.148$ s (compression complete). Horizontal axis is x (m), vertical axis is z (m).

In Fig. 58, the results for the velocity **v** and its components are given.
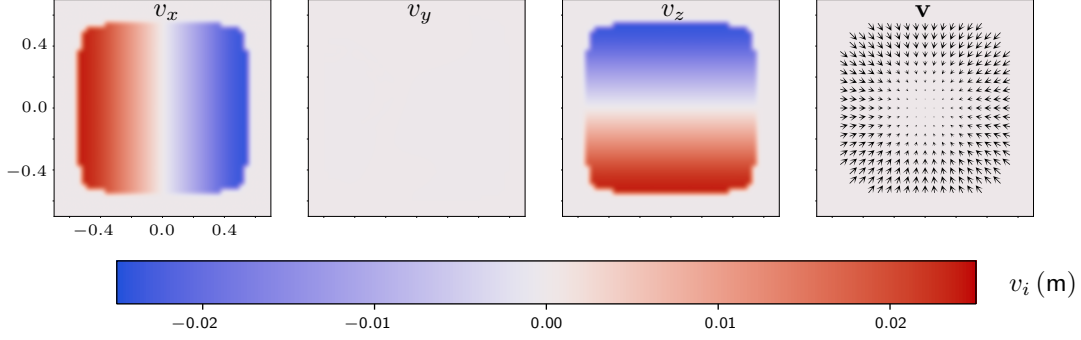
Figure 58 – The magnitude and the components of the velocity $\mathbf{v}$ at $t = 1.148$ s (compression complete). Horizontal axis: x (m), vertical axis: z (m).
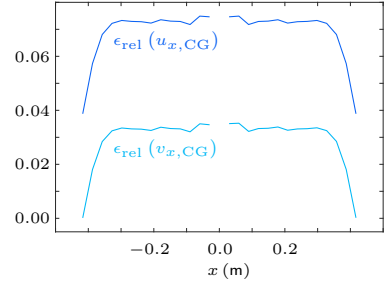
Using the approach as in Section 4.1.1 for the x-component of $\mathbf{u}$ and $\mathbf{v}$, we obtain Figs. 59, 60, and 61.
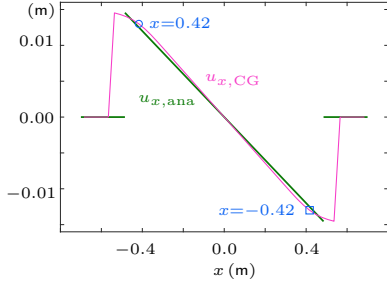
Figure 59 – Displacement components $u_{x,\mathrm{ana}}$ and $u_{x,\mathrm{CG}}$.
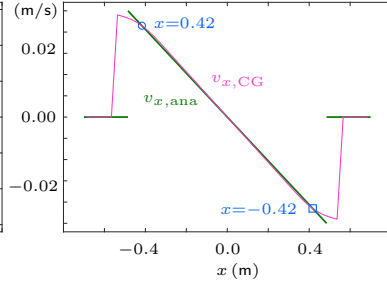
Figure 60 – Velocity components $v_{x,\mathrm{ana}}$ and $v_{x,\mathrm{CG}}$.

Figure 61 – Estimated relative errors $\epsilon_{\mathrm{rel}}(u_{x,\mathrm{CG}})$ for $\epsilon_{\mathrm{rel}}(v_{x,\mathrm{CG}})$.

Using the intervals between the blue circle and square in Figs. 60 and 60, the average of the magnitude of the relative errors are[*]

$$\begin{cases} \bar{\epsilon}_{\mathrm{rel}}(u_{x,\mathrm{CG}}) = 0.029 \pm 0.033, & -0.42 < x < 0.42 \text{ (m)}, \\ \bar{\epsilon}_{\mathrm{rel}}(v_{x,\mathrm{CG}}) = 0.012 \pm 0.014, & -0.42 < x < 0.42 \text{ (m)}, \end{cases}$$

The results for the stress tensor are given in Fig. 62.

---

[*]Since the relative error is infinite at $x = 0$, we use $\max(u_{x,\mathrm{ana}})$ and $\max(v_{x,\mathrm{ana}})$ in the denominator in Eq. (10b), i.e. as reference.
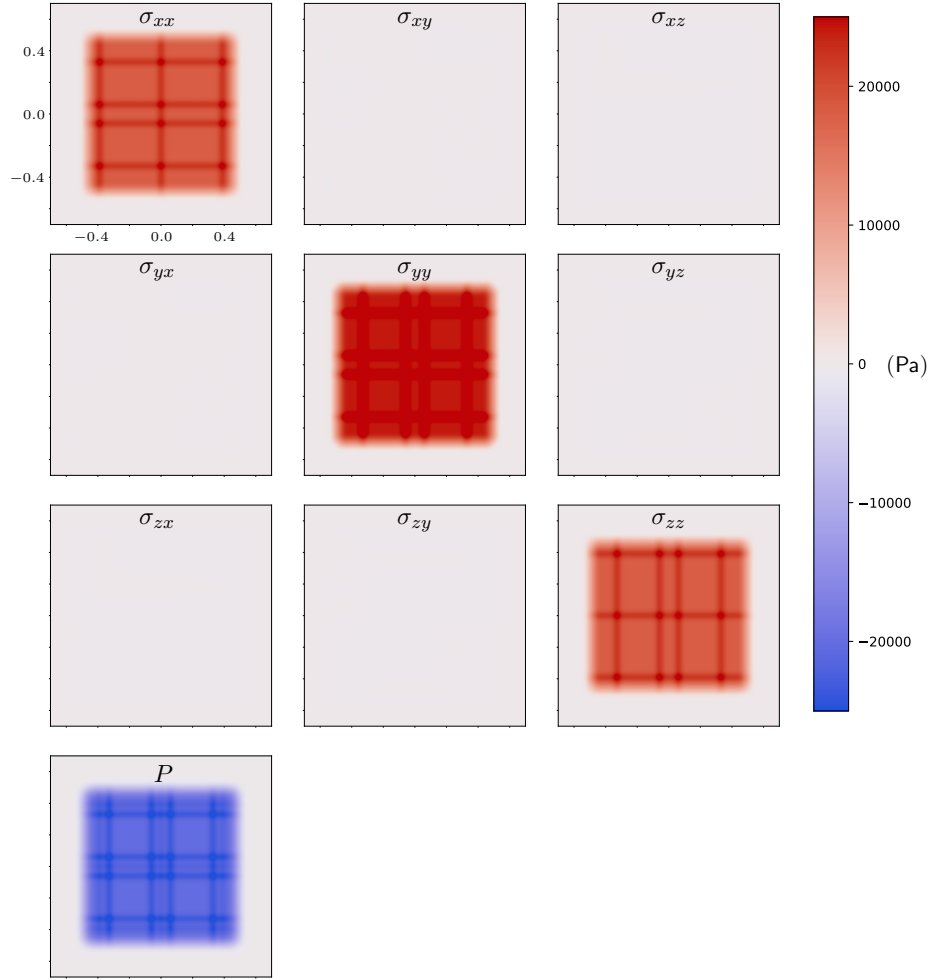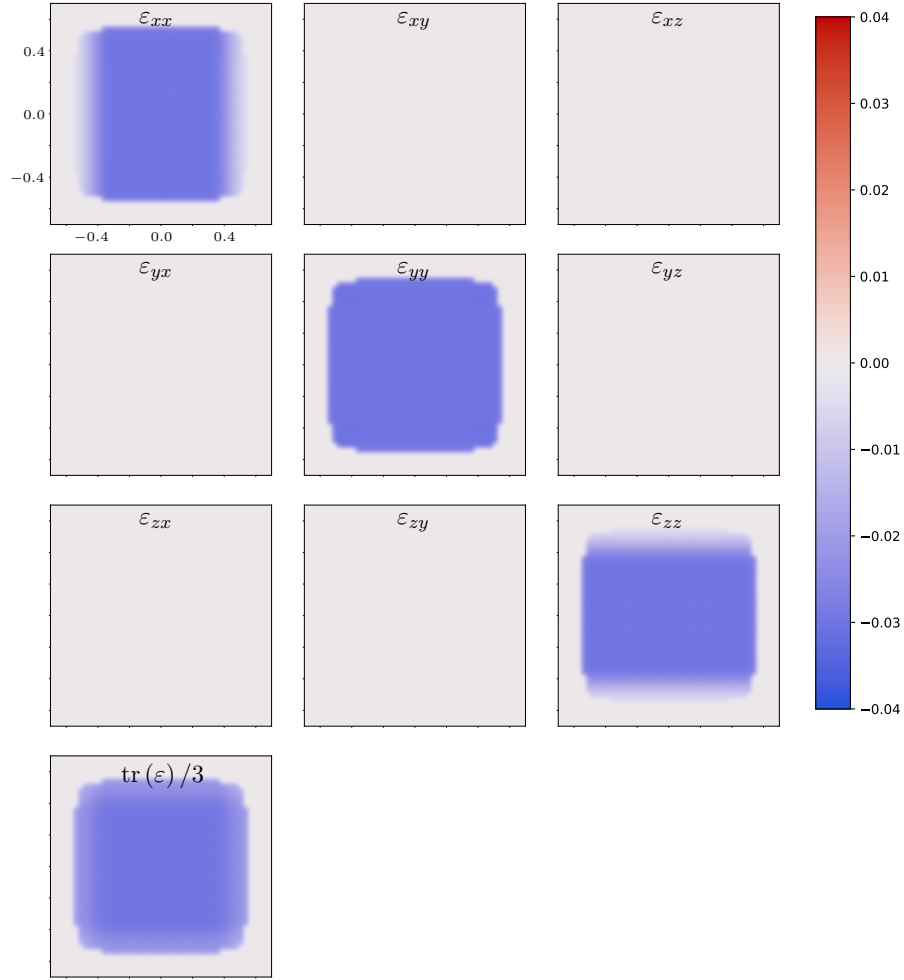
Figure 62 – The components of the stress tensor σ_{ij} at $t = 1.484$ s (compression complete). The horizontal axis is x (m), and the vertical axis is z (m). Note the streaks in the plots.

We note horizontal and vertical streaks in the plots in Fig. 62. These are likely the result of the stress being evaluated over Heaviside cubes and the particles being arranged in a primitive cubic formation—the number of horizontal or vertical particle layers included in a horizontal or vertical Heaviside cube layer varied over the sample, markedly increasing the stress in some rows and columns in the plots. This is not a problem for properly modelled soil due to the granularity of such soil.

In Fig. 62, we note that all non-diagonal components are zero, as expected, since the primitive cubic formation of the sample was preserved throughout the test.

The results for the infinitesimal strain tensor are given in Fig. 63.

Figure 63 – The components of the infinitesimal strain tensor ε_{ij}, and the mean of its trace, at $t = 1.484\,\mathrm{s}$ (compression complete). The horizontal axis is x (m), and the vertical axis is z (m).

In Fig. 63, we note that all non-diagonal components are zero, as expected.

A.4.6 Gravity Test—Particles in Simple Cubic Formation

Using the test sample from Fig. 17, gravity was activated for the particles (but not the walls). The sample was consequently compressed under its own weight, see Fig. 65. By visually studying the simulation, one notices that the particle layers parallel to the xy-plane bounced like bouncing balls—the maximum height reached decreased after each bounce as a result of the dissipation of energy due to the damping of the normal forces. Due to the confining side walls the simple cubic formation was preserved during the test.
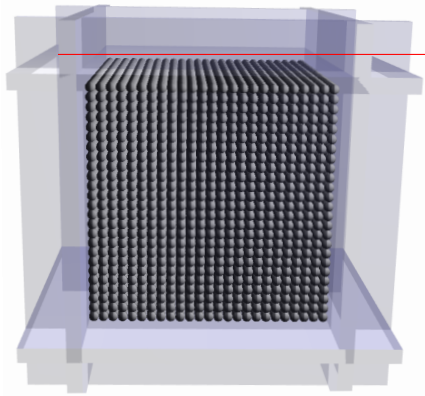
Figure 64 – The test sample at $t = 0$ s (same as Fig. 17).
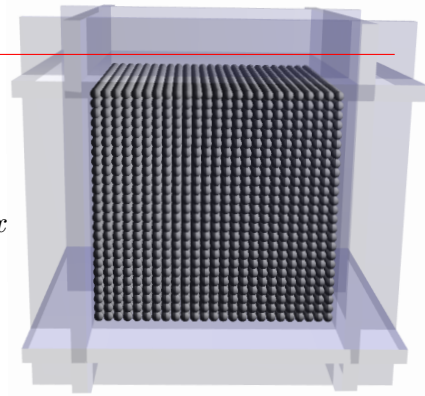
Figure 65 – The test sample at $t = 2.4$ s (equilibrium).

After a relaxation time of 2 s, we set the mass of the top wall to 0.1 kg and accelerated the wall slowly towards the sample, with an allowed maximum force of 0.1 N.* When the wall reached the sample it was unable to move farther because of the force constraint, unless the sample continued to be compressed due to gravity. When the top wall had moved no more than 0.1 cm (1/20 of the particle radius) during 500 timesteps, equilibrium was considered to have been reached and the test was finished. The function of the top wall was to determine when equilibrium was reached and to measure the compression of the sample.

Results for the particle displacement **u** and its components is given in Fig. 66.
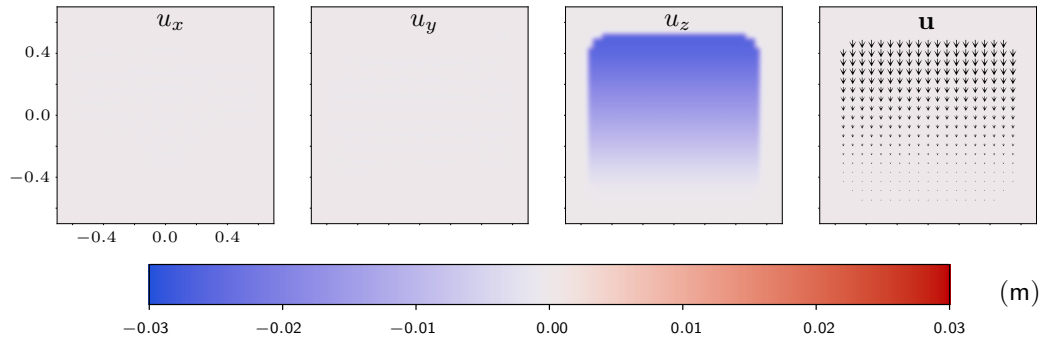
Figure 66 – The components of the particle displacement **u** at $t = 2.4$ s (at equilibrium). The horizontal axis is x (m), and the vertical axis is z (m).

We note that the plots in Fig. 66 agree well with Eq. (11d).

At the start of the test, the top wall just grazed the top particle layer in the sample. At the end of the test, the top wall also just grazed the top layer of the sample. Thus, the top wall moved the same distance as the top layer. By storing the position of the top wall at the first and last timestep, we could determine the distance the top layer had travelled (according to the AGX software), which we denote $u_{z,\text{AGX}}$. Also, by analyzing

---

*Since the mass and force were very low, the increased pressure on the sample due to the top wall was surely negligible.

the numerical CG data, we obtain the same distance, as estimated by CG, which we denote $u_{z,\mathrm{CG}}$. We assume that $u_{z,\mathrm{AGX}}$ is the true distance travelled. We then obtain the following absolute and relative errors for the displacement in the z-direction:

$$\begin{cases} \epsilon_{\mathrm{abs}}\left(u_{z,\mathrm{CG}}\right) = -5.5 \times 10^{-4} \text{ m}, \\ \epsilon_{\mathrm{rel}}\left(u_{z,\mathrm{CG}}\right) = -0.021. \end{cases}$$

The results for the components of the stress tensor σ_{ij} are given in Fig. 67.
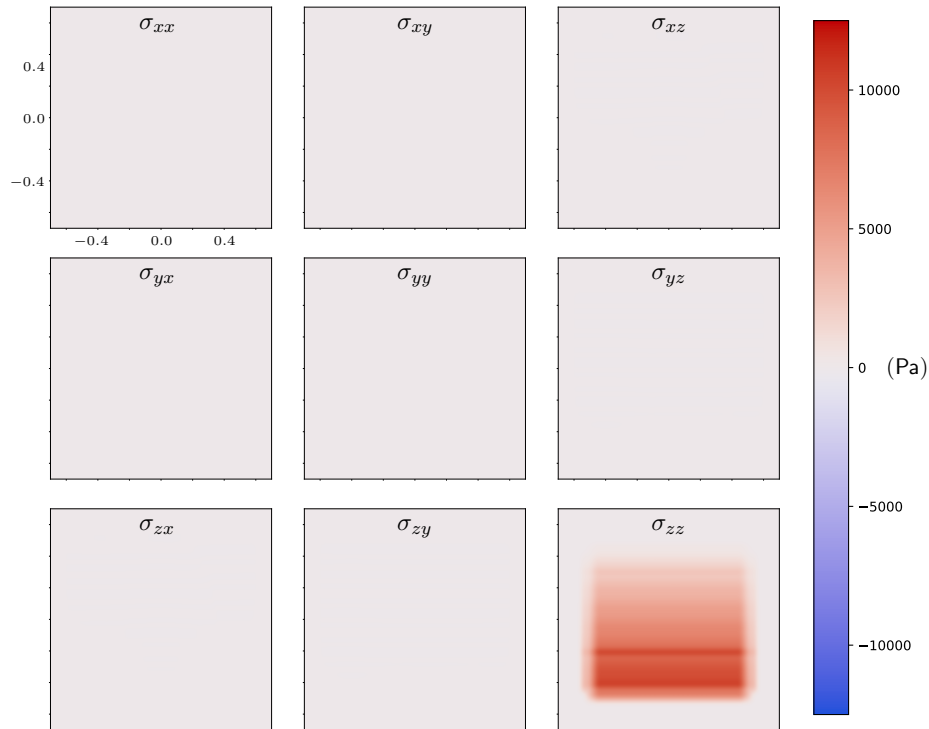
Figure 67 – The components of the stress tensor σ_{ij} at $t = 2.4$ s. Horizontal axis is x (m), vertical axis is z (m). Notice the horizontal streak in σ_{zz}.

Notice the streak in σ_{zz} in Fig. 67. See the text below Fig. 62 for a comment on this. The results of the infinitesimal strain tensor ε_{ij} are given in Fig. 68.

Figure 68 – The components of the infinitesimal strain tensor ε_{ij} at $t = 2.4$ s. Horizontal axis is x (m), vertical axis is z (m).

The plots in Fig. 68 are expected. The compression is a function of only z, and only in the z-direction—all components should therefore be zero except ε_{zz}, see Eq. (13d).

A.4.7 Gravity Test—Particles in Random Configuration

This is the same test as in Section A.4.6, but now the test sample in Fig. 18 was used. As with the test with the simple cubic formation, the particles bounced somewhat like bouncing balls, but this time—due to the random particle configuration—the movement of the particles was obviously more irregular.
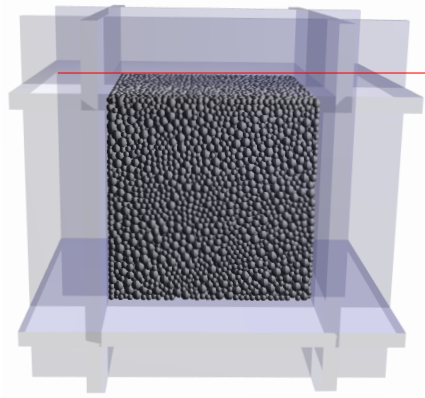
Figure 69 – The test sample at $t = 0$ s (same as Fig. 18).
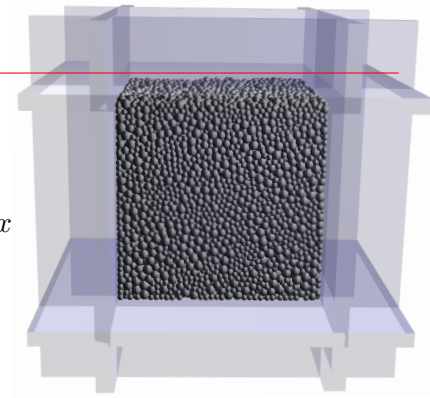
**Figure 70** – The test sample at $t = 2.4$ s (at equilibrium).

The results for the particle displacement $\mathbf{u}$ and its components are given in Fig. 71.
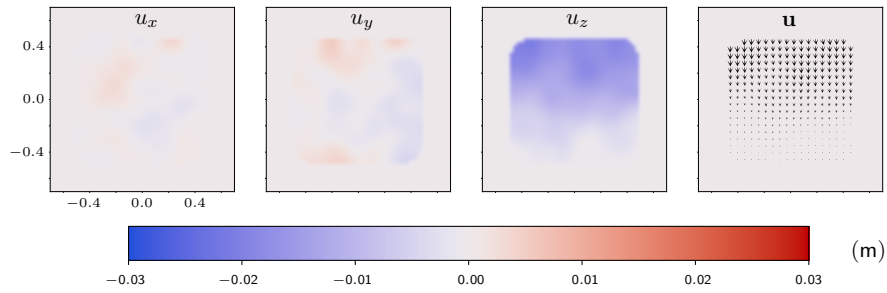
Figure 71 – The components of the displacement $\mathbf{u}$ at $t = 2.4$ s (at equilibrium). Horizontal axis is x (m), vertical axis is z (m).

We see that the plots in Fig. 71 agree quite well with Eq. (11d). Expectedly—due to the random configuration—they do not agree with the equation as well as the plots in Fig. 66 do.

The result for the stress tensor σ_{ij} and the pressure P are given in Fig. 72.
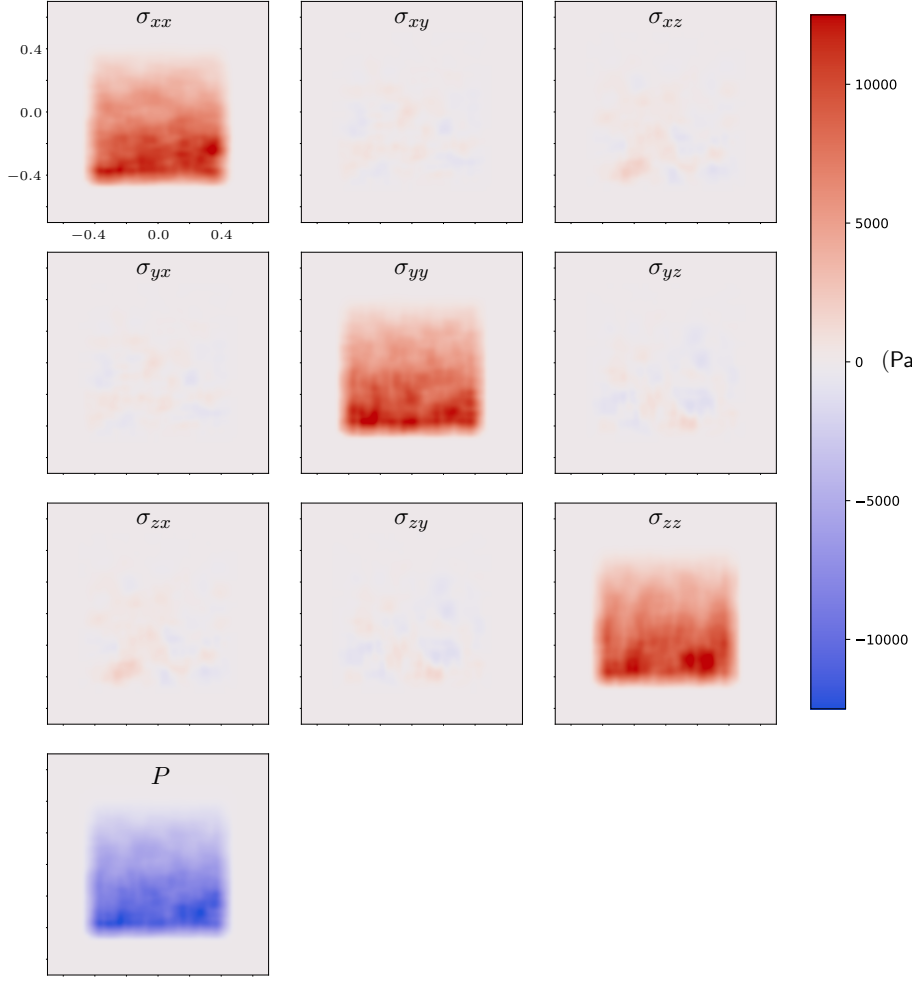
Figure 72 – The components of the stress tensor σ_{ij} and the pressure P at $t = 2.4$ s. Horizontal axis is x (m), vertical axis is z (m).

The hydrostatic pressure generated within a liquid of uniform mass density by its own weight is given by [28]:

$$P = \rho g h, \tag{15}$$

where ρ is the mass density of the liquid, g the gravitational acceleration, and h the vertical distance from the point of interest to the surface of the liquid.

By considering the mass and dimensions of the sample, and treating it like a liquid, we obtain, by Eq. (15), an analytical function for the pressure as a function of z (at equilibrium), denoted $P_{z,\text{ana}}$. Also, we compute the average* pressure given by the CG data as a function of z, and denote this function $P_{z,\text{CG}}$. In Fig. 73, $P_{z,\text{ana}}$ and $P_{z,\text{CG}}$ are compared. Moreover, at $z = -0.34$ m, we compute the analytic static pressure and denote this pressure $P_{t,\text{ana}}$. Furthermore, at $z = -0.34$, we compute the average pressure

---

*The width (along x) of the averaged section is the same as the width of the black square in Fig. 24.
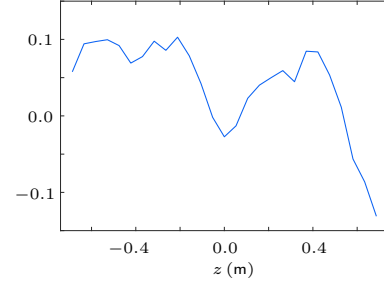
from the CG data as a function of time and denote this function $P_{t,\mathrm{CG}}$. In Fig. 74, we compare $P_{t,\mathrm{ana}}$ and $P_{t,\mathrm{CG}}$. The relative error for $P_{z,\mathrm{CG}}$, using the interval between the blue circle and square in Fig. 73, is given in Fig. 75.
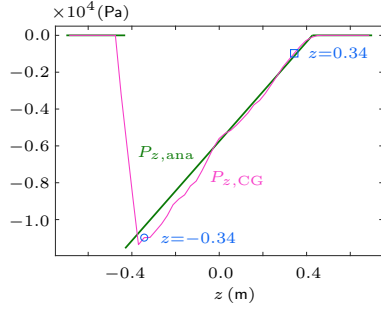
Figure 73 – Pressures $P_{z,\mathrm{ana}}$ and $P_{z,\mathrm{CG}}$ at $t = 2.4$ s.
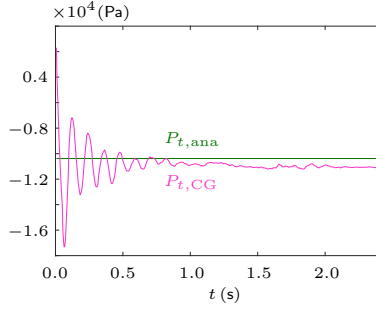
Figure 74 – Pressures $P_{t,\mathrm{ana}}$ and $P_{t,\mathrm{CG}}$, both at $z = -0.34$, the latter of which is a function of time.

Figure 75 – Estimated relative error for ϵ_{abs} for $P_{z,\mathrm{CG}}$.

In Figs. 73 and 74, we note that the *CG*-functions follow the analytical functions quite close.

Using the interval between the blue circle and square in Fig. 73, The average of the magnitude of the relative errors for $P_{z,\mathrm{CG}}$ is

$$\bar{\epsilon}_{\mathrm{rel}}\left(P_{z,\mathrm{CG}}\right) = 0.065 \pm 0.060, \qquad -0.34 < z < 0.34 \ (\mathrm{m}).$$

At $t = 2.4$ s, the relative error for $P_{t,\mathrm{CG}}$ is

$$\epsilon_{\mathrm{rel}}\left(P_{t,\mathrm{CG}}(-34)\right) = 0.059.$$

The results for the infinitesimal strain tensor ε_{ij} and the mean of ε_{ij} $(i = j)$ are given in Fig. 76.
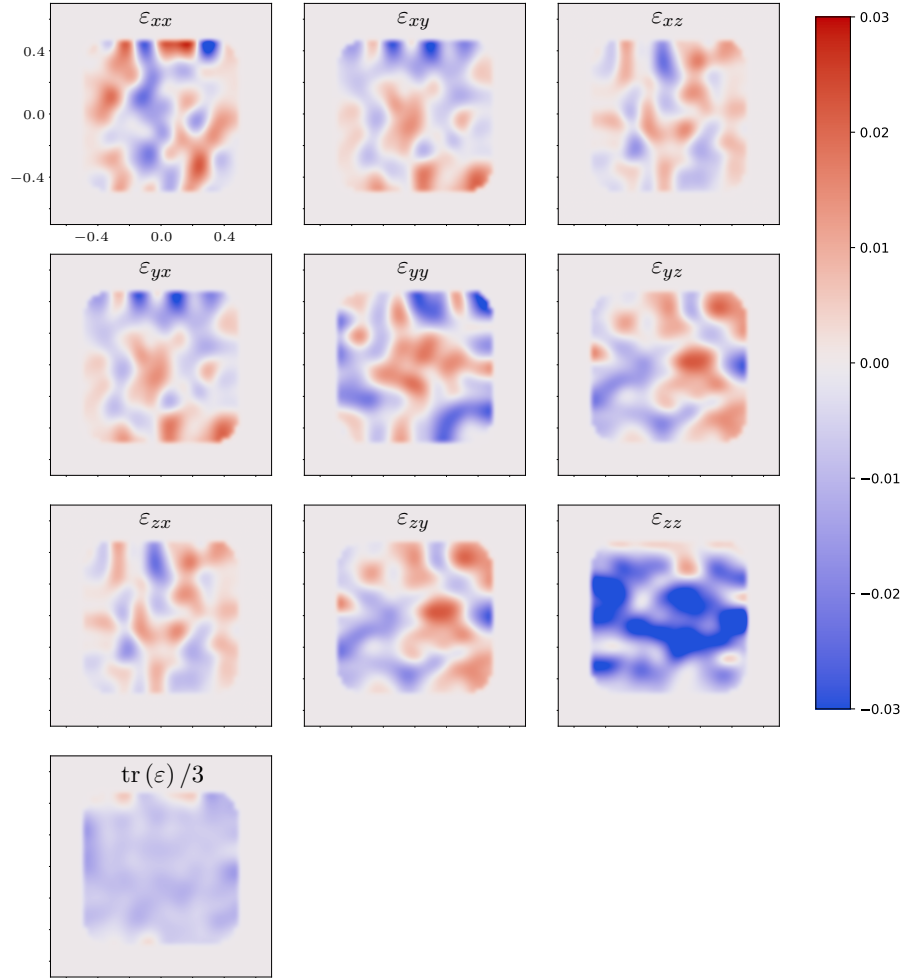
Figure 76 – The components of the infinitesimal strain tensor ε_{ij}, and the mean of ε_{ij} $(i = j)$, i.e $\text{tr}(\varepsilon)/3$, at $t = 2.4$ s. Horizontal axis is x (m), vertical axis is z (m).

By Eq. (13d), all components ε_{ij} in Fig. 76 should be zero, except for ε_{zz}. We see that this is not the case. The components ε_{ij} $(i, j \neq z)$ being non-zero is likely due to the disordered movement of the particles during the gravitational compression.

The result for the mean normal strain rate $\text{tr}(\dot{\varepsilon})/3$ is given in Fig. 77.
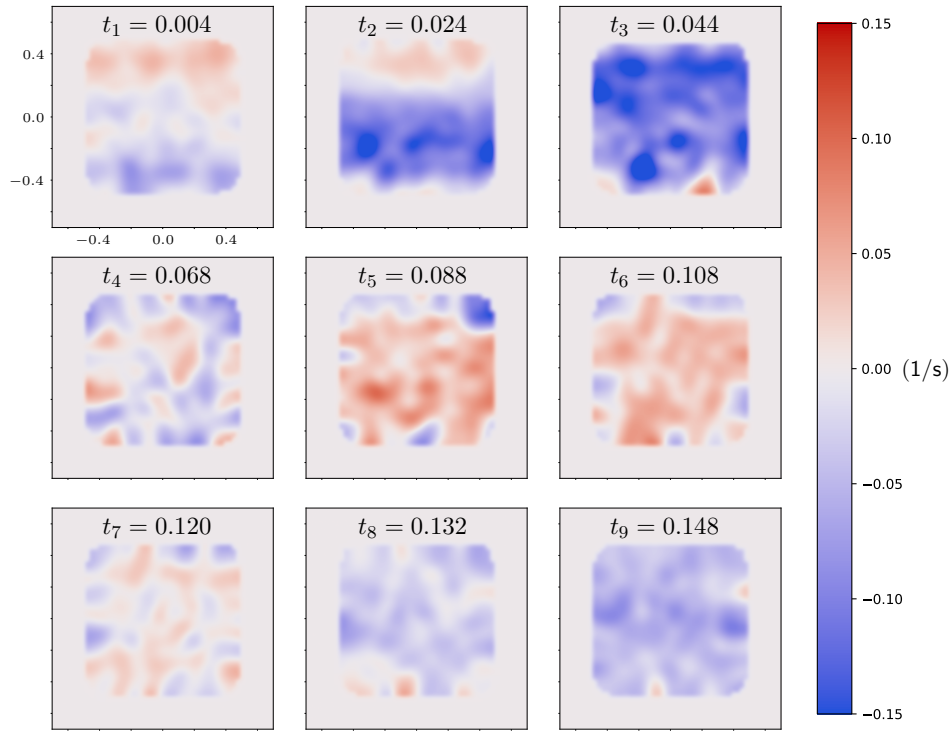
Figure 77 – The mean normal strain rate, i.e. $\mathrm{tr}\,(\dot{\varepsilon})\,/3$, at various time (s). Horizontal axis is x (m), vertical axis is z (m).
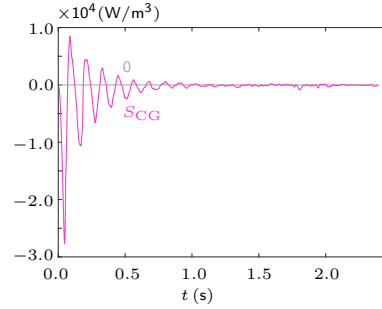
The results for the power density, with velocity vector fields superimposed, are given in Fig. 78.
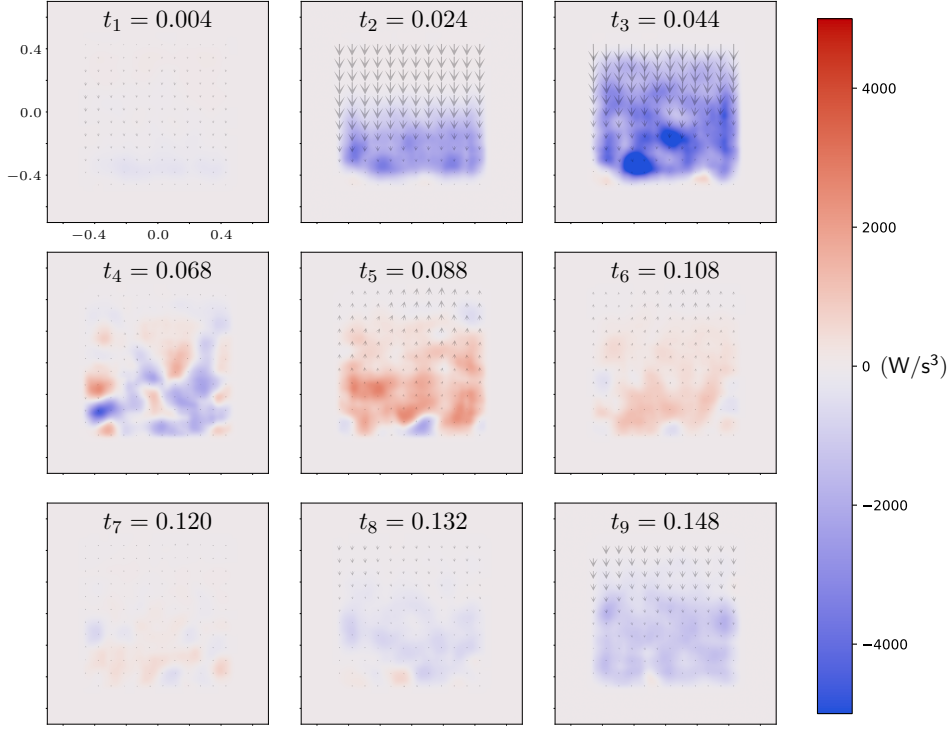
Figure 78 – The power density at the same times (s) as in Fig. 77. The shaded arrows are the velocity vector fields. Horizontal axis is x (m), vertical axis is z (m).

The plots in Fig. 77 are quite similar to those in Fig. 78. Also, the plots in both these figures makes sense. At times t_2 and t_3, the velocities were in the downward direction. Thus, at those times, the sample was being compressed, and consequently energy was added to the sample. As expected, at those times, a negative mean normal strain rate is seen in 77 (indicating compressing) and a negative power density is seen in 78 (indicating the addition of energy to the sample). At t_5 and t_6, the veloc-

Figure 79 – S_{CG} with a reference line at 0 W/m^3.

ities were in the upward direction, so at those times, the sample expanded and energy was being released from the sample. This is also reflected in the plots. Finally, at t_8 and t_9, the sample was being compressed again.

We let S_{CG} be the average of the power density, based on the CG-data, see Fig. 79. By integrating S_{CG} numerically from $t = 0$ to $t = t_{\mathrm{end}}$, and dividing by the volume* of the sample, we obtain the energy transferred to the sample due to the compression due to gravity. We denote this energy E_S. Now, we consider the bottom of the sample to have been located at $z = 0$. Also, at the start of the test, we let the height of the sample

---

*We take the average of the initial volume and the estimated final volume. The change in volume is very small.

be h_0. Thus, at that time, the mass center of the sample was approximately located at $z = h_0/2$. At the end of the test, the average height of the sample had decreased by some distance Δz_{top}. Thus, at that time, the mass center of the sample was located at $z = (h_0 - \Delta z_{\text{top}})/2$. So, the *mass center* had moved by the distance $\Delta z_{\text{mass}} = \Delta z_{\text{top}}/2$ during the test. So, by assuming that all particles had zero velocity at the end, we have

$$\frac{mgz_{\text{top}}}{2} = E_S + \Delta E_E \qquad \Longleftrightarrow \qquad \Delta z_{\text{top}} = \frac{2\left(E_S + \Delta E_E\right)}{mg},$$

where ΔE_E is the increase in elastic energy in the particles due to the increased compression. If $\Delta E_E = 0$, then

$$\Delta z_{\text{top}} = -0.98 R_{\text{particle}},$$

where R_{particle} is the largest particle radius. By visually inspecting Figs. 69 and 70, we see that this seems a little low: the top of the sample moved perhaps twice this distance. However, not all the energy dissipated, so $\Delta E_E < 0$, yielding $\Delta z_{\text{top}} < -0.98 R_{\text{particle}}$.

The simulations images, corresponding to the times in Figs. 77 and 78, are given in Fig. 80.
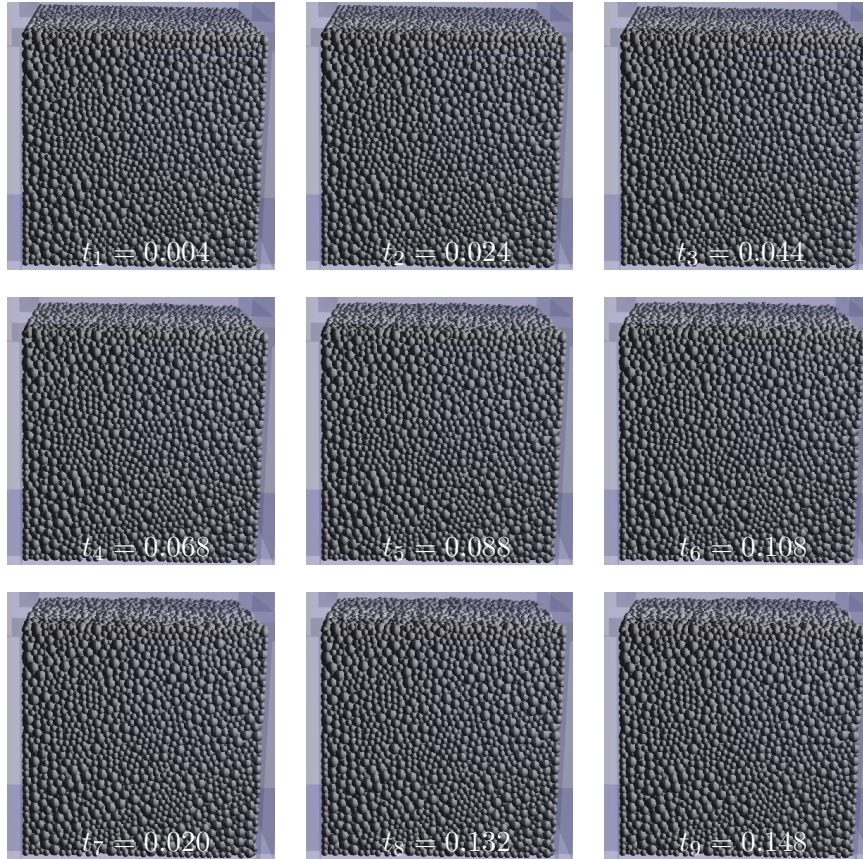
Figure 80 – The simulation images for the gravitational test with particles in random configuration at various times (s). Horizontal axis is x (m), vertical axis is z (m).

Although barely visible, we note in Fig. 80 that the sample was compressed from time t_1 to t_3.

A.4.8 Triaxial Test—Particles in Random Configuration

In this test, the test sample was first loaded into the test-script and the walls were held static for 0.5 s, allowing for any motion of the particles in the test sample to subside. Subsequently, all six walls accelerated slowly towards the origin, as in the isotropic compression test. However, the maximum allowed force for the motors moving the top and bottom walls was essentially infinite, while the motors for the left, right, back, and front walls were constrained to apply a maximum force such that the pressure on the left, right, back, and front surfaces did not exceed 1 kPA (more precisely, the force applied on such a wall was at maximum 1 kPa times the side area of the sample in contact with that wall). The instruction was that, if the constraint was satisfied, the speed of the walls was increased linearly each timestep with 0.01 cm/s until the speed 2.5 cms/s was reached at which point that speed was maintained. As the top and bottom walls had no constraint with respect to sample pressure, they compressed the sample, increasing the pressure. In order for the other walls to also compress the sample, they would have had to apply a force such that the pressure exceeded 1 kPa. Since this was not allowed, these walls moved away from the origin, expanding the sample in the x- and y-directions. When the decrease in sample length in the z-direction was 10 % the test was finished.

This is known as a triaxial test, and its physical equivalent is used to investigate the failure of soil under shear [5].
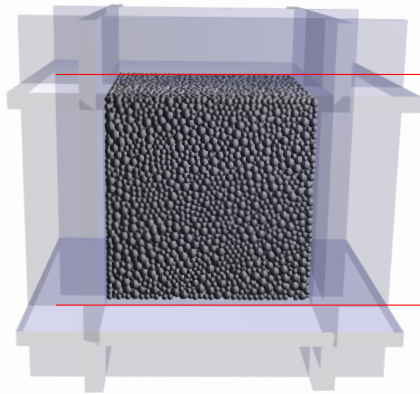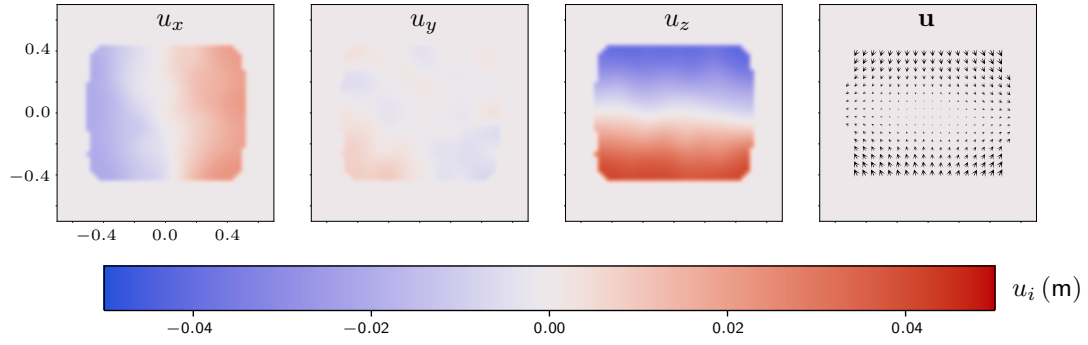

Figure 81 – The test sample at $t = 0$ s (same sample as Fig. 18).
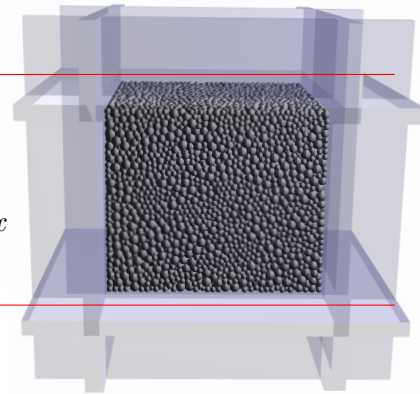
Figure 82 – The test sample at $t = 2.264$ s (test complete).

Results for the particle displacement $\mathbf{u}$ and its components are given in Fig. 83.
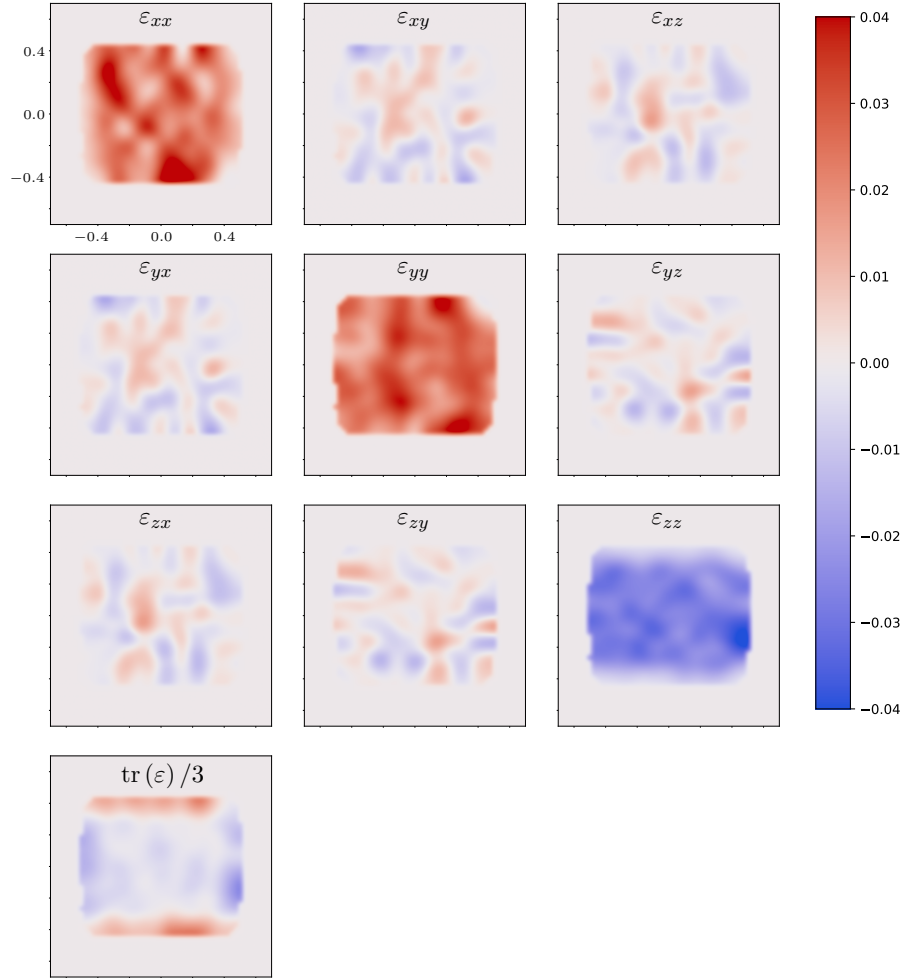
Figure 83 – The magnitude and the components of the particle displacement **u** at $t = 2.264$ s (test complete). Horizontal axis: x (m), vertical axis: z (m).

The plots in Fig. 83 are consistent with Eq. (11b).

Results for the infinitesimal strain tensor are given in Fig. 84.

Figure 84 – The components of the infinitesimal strain tensor ε_{ij}, and the mean of ε_{ii} at $t = 2.264$ s (compression complete). The horizontal axis is x (m), and the vertical axis is z (m).

Since there was expansion in the x- and y-direction, we expect ε_{xx} and ε_{yy} to be positive, and since there was compression in the z-direction, we expect ε_{zz} to be negative. This is also what is seen in Fig. 84. We let $\varepsilon_{ii,\mathrm{AGX}}$ $(i = x, y, z)$ be the tensor components based on the AGX-data. Also, we let $\varepsilon_{ii,\mathrm{CG}}$ $(i = x, y, z)$ be the corresponding averaged components based on the CG-data. Assuming that $\varepsilon_{ii,\mathrm{AGX}}$ are the true components, we obtain Figs. 85, 86, 87.
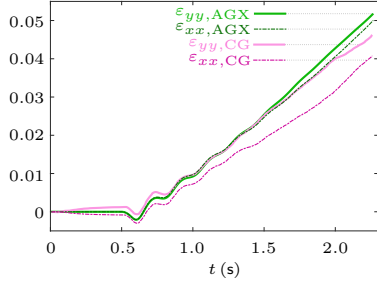
Figure 85 – Strain tensor components $\varepsilon_{xx,\text{AGX}}$, $\varepsilon_{yy,\text{AGX}}$, and $\varepsilon_{xx,\text{CG}}$, $\varepsilon_{yy,\text{CG}}$.
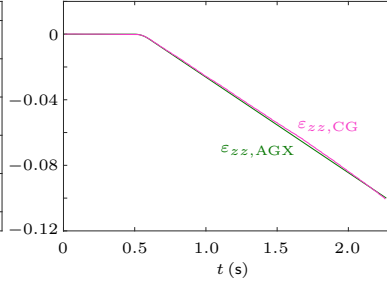
Figure 86 – $\varepsilon_{zz,\text{AGX}}$ and $\varepsilon_{zz,\text{CG}}$.
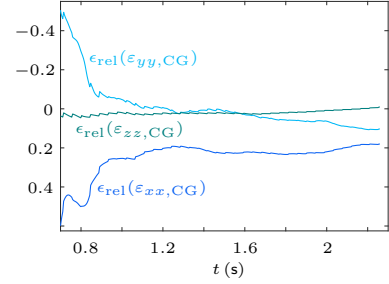
**Figure 87** – Estimated relative errors for $\varepsilon_{ii,\text{CG}}$.

The average of the magnitudes of the relative errors are

$$
\begin{cases}
\overline{\epsilon}_{\text{rel}}(\varepsilon_{xx,\text{CG}}) = 0.25 \pm 0.08, & t > 0.7 \text{ s}, \\
\overline{\epsilon}_{\text{rel}}(\varepsilon_{yy,\text{CG}}) = 0.073 \pm 0.122, & t > 0.7 \text{ s}, \\
\overline{\epsilon}_{\text{rel}}(\varepsilon_{zz,\text{CG}}) = 0.021 \pm 0.011, & t > 0.7 \text{ s}.
\end{cases}
$$

We note that $\overline{\epsilon}_{\text{rel}}(\varepsilon_{xx,\text{CG}})$ is markedly larger than $\overline{\epsilon}_{\text{rel}}(\varepsilon_{yy,\text{CG}})$ even though the expansion in the x-direction is very similar to the expansion in the y-direction. The discrepancy is related to the voxel-grid—in the x-direction, the number of voxel is far greater than in the y-direction, i.e. $N \gg 3$, see Fig. 19.

A.4.9 Shear Test—Particles in Random Configuration

In this test, we affixed cylindrical rigid bodies (yellow) at the center of the left and right walls (purple), see Fig. 88. The cylinders and walls could not collide with each other. All walls were held static except for the left and right walls. After a relaxation time of 0.5 s, the left and right walls started to rotate clockwise about an axis going through the cylinders. The angular speed increased linearly each timestep by 2×10^{-4} rad/s. When a wall obtained the angular speed 0.05 rad/s that speed was maintained until the rotation was 3°, upon which that wall was set to static. When both walls reached a rotation of a 3°, the test finished, see Fig. 89.
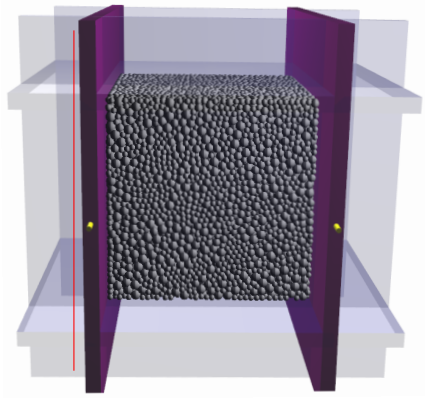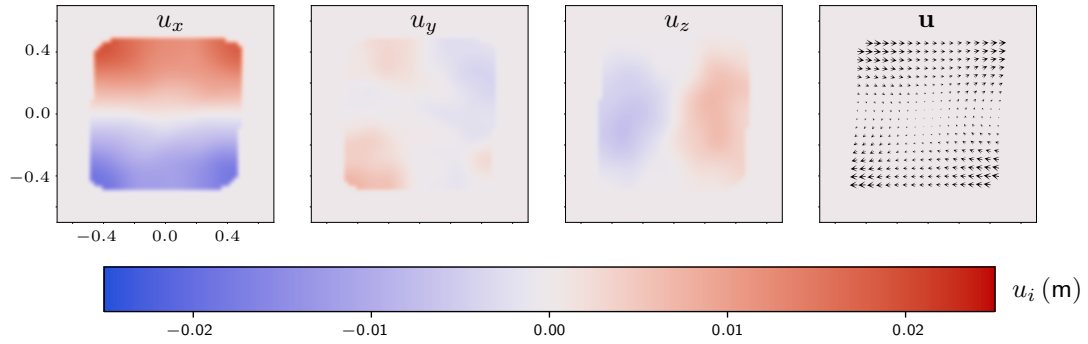
Figure 88 – The test sample at $t = 0$ s (same sample as Fig. 18), with the left and right walls coloured purple.
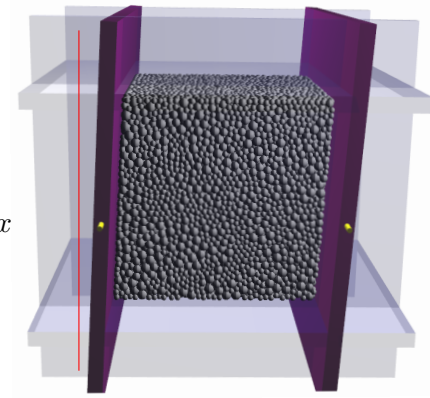
**Figure 89** – The test sample at $t = 1.6$ s (test complete).

Results for the particle displacement **u** and its components are given in Fig. 83.

Figure 90 – The magnitude and the components of the particle displacement **u** at $t = 1.6$ s (test complete). Horizontal axis is x (m), vertical axis is z (m).

The plots in 90 agree quite well with Eq. (11c), although the components that are analytically zero are experimentally non-zero.
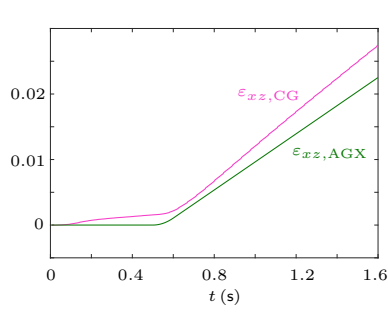
Results for the infinitesimal strain tensor is given in Fig. 91.
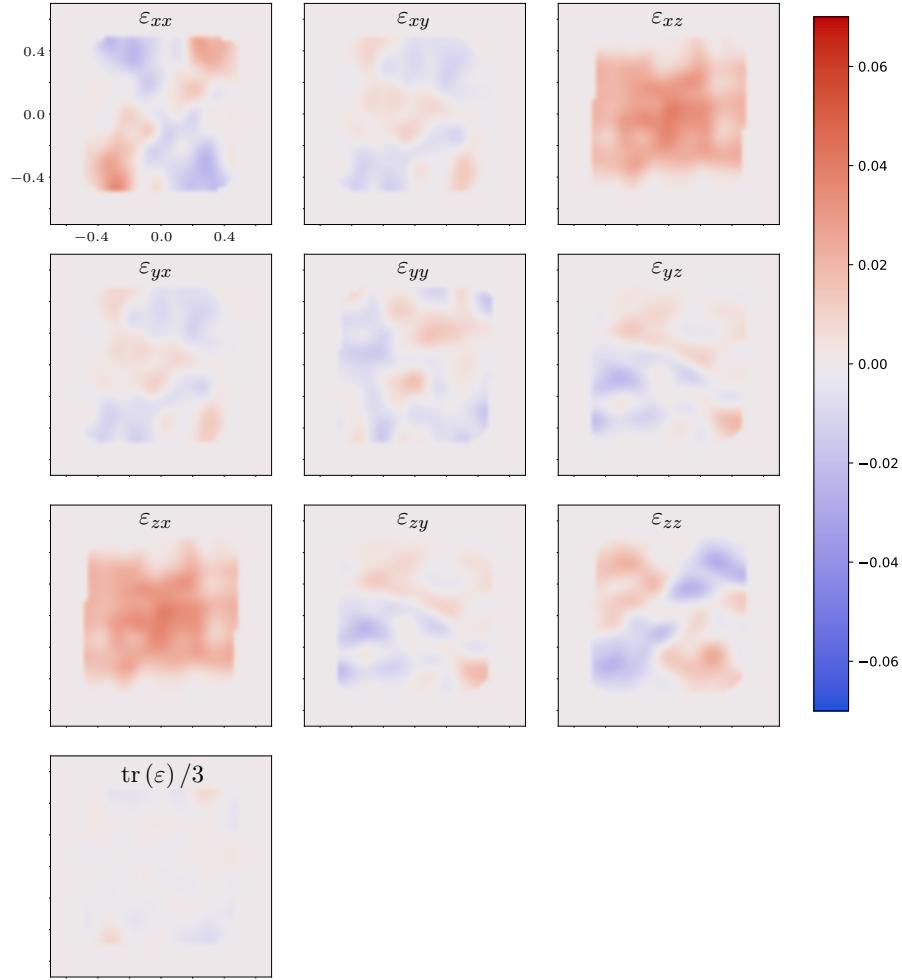
Figure 91 – The components of the infinitesimal strain tensor ε_{ij}, and the mean of its trace, at $t = 1.6$ s (shearing deformation complete). The horizontal axis is x (m), and the vertical axis is z (m).

As for the displacement, the agreement between the plots in 91 and Eq. (13c) is quite good. Components that are analytically zero are experimentally non-zero, however.
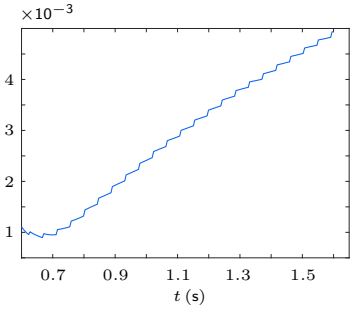
We let $\varepsilon_{xz,\text{AGX}}$ be the tensor component based on the AGX-data, and we let $\varepsilon_{xz,\text{CG}}$ be the averaged component based on the CG-data. Assuming that $\varepsilon_{xz,\text{AGX}}$ is the true quantity, we obtain Figs. 92, 93, and 94.

Figure 92 – Infinitesimal strain tensor components $\varepsilon_{xz,\text{AGX}}$ and $\varepsilon_{xz,\text{CG}}$.
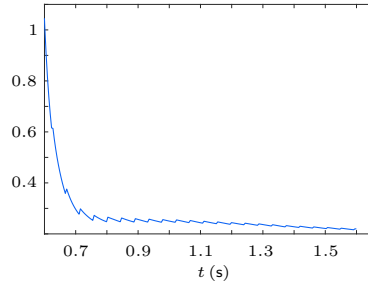
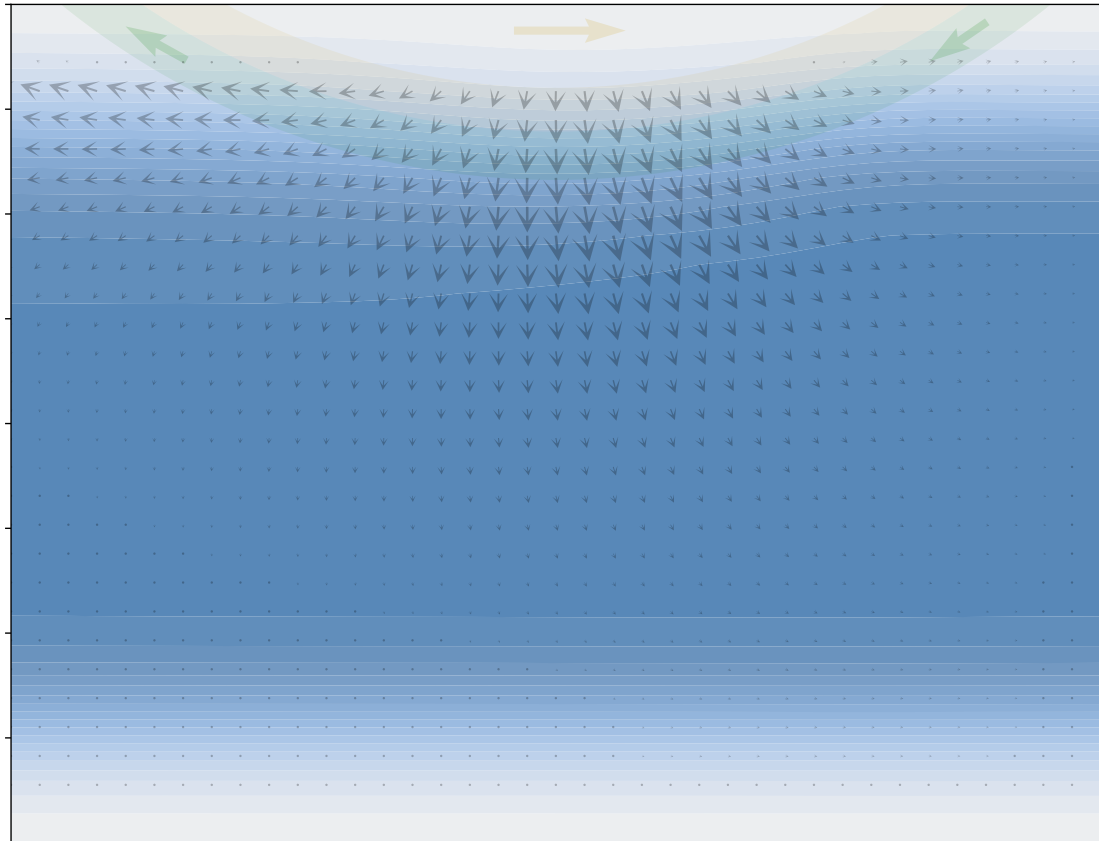**Figure 93** – Estimated relative error for $\varepsilon_{xz,\text{CG}}$

Figure 94 – Estimated absolute error for $\varepsilon_{xz,\text{CG}}$
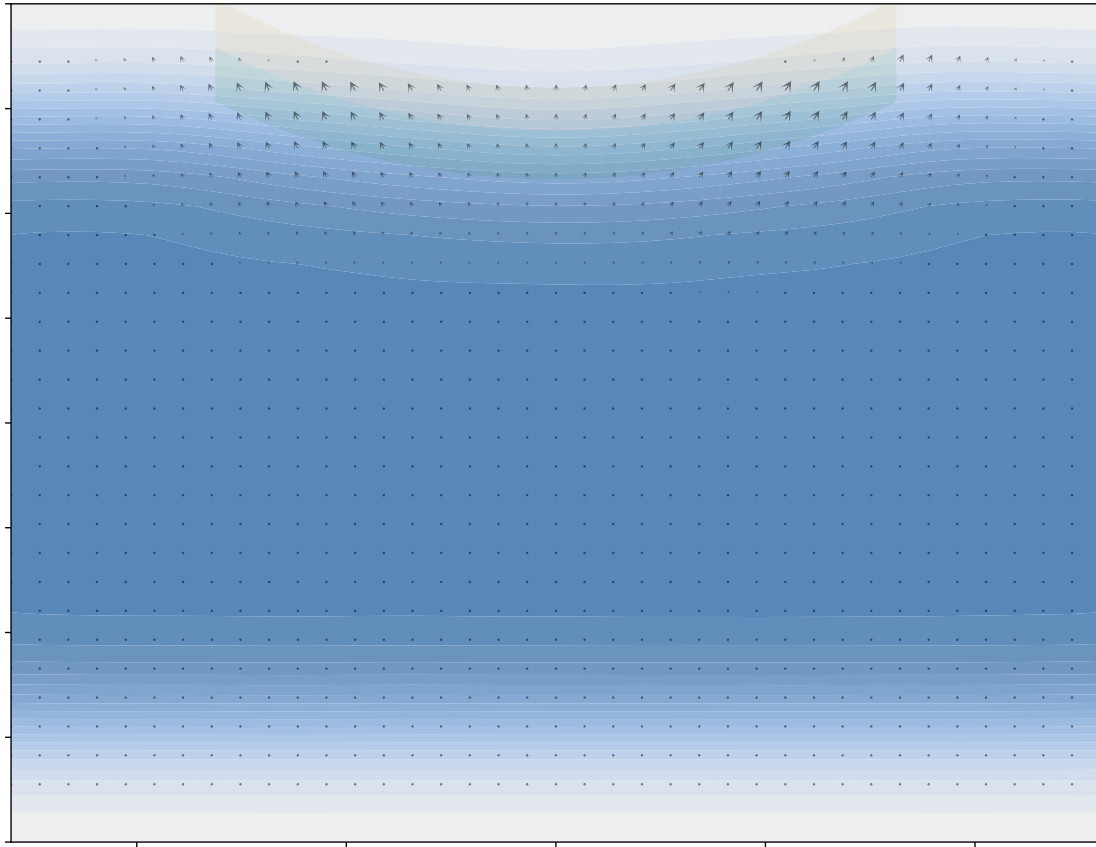
The average magnitude of the relative error is

$$\bar{\epsilon}_{\text{rel}}\left(\varepsilon_{xz,\text{CG}}\right) = 0.27 \pm 0.10, \qquad t > 0.6 \text{ s}.$$

A.4.10   Vehicle on Soil—Density and Displacement

Figure 95 – The time-averaged mass density scalar field and displacement vector field in the xz-plane ($y = 0$) for the vehicle on soil, i.e. a magnification of the top-left plot in Fig. 51.

Figure 96 – The time-averaged mass density scalar field and displacement vector field in the yz-plane ($x = 0$) for the vehicle on soil, i.e. a magnification of the top-left plot in Fig. 52.